JGR Space Physics

RESEARCH ARTICLE
10.1029/2019JA026606

Key Points:
- In magnetotail fast flows, Fermi acceleration creates parallel electron beams that produce oblique whistler waves through a beam instability
- The oblique whistler waves are able to efficiently scatter electrons into the diffuse aurora
- The oblique whistler waves scatter electrons more strongly than the ECH waves into the loss cone

Correspondence to:
D. E. Wendel,
deirdre.e.wendel@nasa.gov

Citation:
Wendel, D. E., Khazanov, G. V., Tripathi, A. K., Singhal, R. P., & Zesta, E. (2019). Source of the bursty bulk flow diffuse aurora: Electrostatic cyclotron harmonic and whistler waves in the coupling of bursty bulk flows to auroral precipitation. *Journal of Geophysical Research: Space Physics*, *124*, 6669–6690. https://doi.org/10.1029/2019JA026606

Received 11 FEB 2019
Accepted 22 JUL 2019
Accepted article online 31 JUL 2019
Published online 13 AUG 2019

Source of the Bursty Bulk Flow Diffuse Aurora: Electrostatic Cyclotron Harmonic and Whistler Waves in the Coupling of Bursty Bulk Flows to Auroral Precipitation

D. E. Wendel[1], G. V. Khazanov[1], A. K. Tripathi[2], R. P. Singhal[2], and E. Zesta[1]

[1]NASA Goddard Space Flight Center, Greenbelt, MD, USA, [2]Department of Physics, Indian Institute of Technology (Banaras Hindu University), Varanasi, India

Abstract Electron cyclotron harmonic (ECH) and whistler chorus waves are recognized as the two mechanisms responsible for the resonant wave-particle interactions necessary to precipitate plasma sheet electrons into the ionosphere, producing the diffuse Aurora. Previous work has demonstrated ECH waves dominate electron scattering at L shells >8, while whistler chorus dominates scattering at L shells $L < 8$. However, we find from Time History of Events and Macroscale (THEMIS) Interactions during Substorms observations of fast flows at $L = 12$ that oblique whistler chorus emissions play the dominant role in scattering electrons. Previous works have identified whistler-mode waves within fast flows that are produced by an electron temperature anisotropy $T_{e,\perp}/T_{e,||} > 1$, consistent with electron betatron acceleration. Here, however, we find whistler chorus emissions throughout an interval of fast flows where $T_{e,\perp}/T_{e,||} < 1$. Parallel electron beams account for the enhanced parallel electron temperature and serve as the instability mechanism for the whistler chorus. The parallel electron beams and associated cigar-shaped distributions are consistent with Fermi acceleration at dipolarizations in fast flows. We demonstrate that the scattering efficiency of the whistler chorus exceeds that of ECH waves, which THEMIS also detects during the fast flows. The obliquity of the whistler waves permits efficient scattering of lower-energy electrons into the diffuse aurora. We conclude that Fermi acceleration of electrons provides one important free-energy source for the wave-particle interactions responsible for coupling plasma sheet electrons into the diffuse aurora during substorm conditions.

1. Introduction

The mechanisms that transport kinetic and electromagnetic energy from the Earth's magnetotail to the ionosphere constitute active areas of investigation. Azimuthally narrow bands of fast flows provide the primary momentum and energy transport in the magnetotail (Angelopoulos et al., 1992, 1994; Baumjohann et al., 1990). Through the precipitation of electrons, the flows deposit energy into the ionosphere to produce poleward boundary intensifications (PBIs), auroral streamers, and discrete and diffuse aurora (Henderson et al., 1998; Lyons et al., 1999; Sergeev et al., 1999, 2000, 2004; Zesta et al., 2000, 2002, 2006) and have been associated with substorm onsets (e.g., Angelopoulos et al., 2008; Zesta et al., 2011). While a number of studies have furnished the mapping of such flows and associated field-aligned currents to the ionosphere (e.g., Kauristie et al., 2000; Shi et al., 2012; Zesta et al., 2011), the precise physical process by which the coupling occurs remains unexplained.

The substorm auroral signatures produced by the ionization from electrons are subdivided into either the *diffuse* or *discrete* aurora. The diffuse aurora comes from electrons with a diffuse emission in a range of energies from approximately 1 eV to 1 keV, while the discrete Aurora arises from electrons with energies above 1 keV that produce intense, localized emissions. The source populations for the responsible accelerated electrons differ in the two cases, with the former scattered from the plasma sheet population by wave-particle interactions, and the latter accelerated from low altitudes below approximately 10,000 km (Evans, 1974) by either Alfven waves or parallel electric fields. The diffuse aurora is found near the more equatorward part (Liang, Ni, et al., 2011; Liang, Spanswick, et al., 2011) and sometimes eastward (postmidnight) of the discrete aurora (Kepko et al., 2009), while the discrete aurora defines the more poleward portions of PBIs and streamers. Field lines of both structures map to the fast flows in the magnetotail.

In this study we concern ourselves with the wave scattering mechanism in the plasma sheet fast flows that produces the diffuse aurora. Recent statistical observations and theoretical predictions support the importance, and even dominance, of the whistler chorus in scattering energetic electrons out of the plasma sheet for L shells $\leq$8 (Li et al., 2005; Ni & Thorne, 2012; Santolik et al., 2009; Thorne et al., 2010). Kasahara et al. (2018) measure correlations between plasma sheet electron fluxes into the loss cone, whistler chorus, and pulsating aurora at about $L = 6$. Other observed statistics support the dominant scattering effect of electron cyclotron harmonic (ECH) waves at L shells > 8 (Liang et al., 2010; Ni, Thorne, Liang, et al., 2011; Ni et al., 2012; Zhang et al., 2015) and an association between intense auroral forms and ECH waves at about $L = 6$ (Fuzikawa et al., 2018). However, evidence exists of the importance of VLF whistler waves on the auroral emissions during substorm conditions. Most researchers have detected whistler waves in the magnetic flux pileup regions of fast flows at $L > 8$, where strong magnetic gradients accelerate electrons producing the condition $T_{e,\perp}/T_{e,||} > 1$, where $T_{e,\perp}$ and $T_{e,||}$are the perpendicular and parallel electron temperatures (Deng et al., 2010; Fu et al., 2014; Huang et al., 2012; Khotyaintsev et al., 2011; Panov et al., 2013; Viberg et al., 2014; Zhima et al., 2015). Jiang et al. (2012) found generally heightened VLF wave activity during fast flows at $L > 12$. They determined that flows meeting their criteria for *fast* ($B_z > \sqrt{B_x^2 + B_y^2}$, average $E_y > 1$ mV/m, peak $E_y > 2$ mV/m, average bulk $v_x > 140$ km/s, and peak $v_x > 200$ km/s) were more likely to have positive electron anisotropy ($T_{e,\perp}/T_{e,||} > 1$), while weaker flows were more likely associated with negative anisotropy ($T_{e,\perp}/T_{e,||} > 1$).

Electron distributions with $T_{e,\perp}/T_{e,||} > 1$ are consistent with betatron acceleration, whereby a gradient in the magnetic field accelerates electrons perpendicular to the magnetic field B through conservation of the first adiabatic invariant $\mu \propto {v_{e,\perp}}^2/B$, where $v_{e,\perp}$ is the perpendicular electron velocity and B is the magnetic field magnitude. Khotyaintsev et al. (2011) find quasi-parallel whistlers that have high-scattering efficiency at the flux pileup regions under such conditions. A recent Time History of Events and Macroscale Interactions during Substorms (THEMIS) study of fast bursty bulk flows at $L = 9$ reveals that quasi-parallel whistler waves produced in the fast flows associated with dipolarization fronts are able to resonate with and scatter 2–26 keV electrons (Zhima et al., 2015). The study determined that the pancake-like anisotropic electron distributions near the edge of the magnetic depressions behind dipolarization fronts provide the free energy for the whistler instability. This is in contrast to other studies that found the waves were produced within the magnetic depressions (Khotyaintsev et al., 2011; Tsurutani et al., 2009). Tagirov et al. (1999) observe VLF chorus emissions in concert with auroral pulsations in the morning sector during substorm activity, based on ground-based VLF recordings and optical measurements in Sodankylä, Finland. One study (Hwang et al., 2014) also discovers electron cigar distributions in association with the production of whistler waves in the dipolarized magnetotail. Our present paper confirms this interpretation. However, the Hwang et al. (2014) work focuses on the role that the ensuing whistler chorus play in ion heating behind dipolarization fronts, whereas our work addresses the question of scattering and coupling to the aurora.

Here we present ECH and whistler wave analysis from THEMIS observations of tail bursty bulk flows at geocentric solar ecliptic (GSE) coordinate $x_{GSE} \sim 11\ R_E$ previously reported by Kepko et al. (2009) in a study of equatorward moving auroral signatures. We wish to determine which waves—ECH or whistlers—have the strongest scattering efficiency from the plasma sheet into the diffuse aurora, and which mechanisms within the fast flows produce the resonant waves.

2. Data and Methodology

On 25 February 2008, THEMIS D and THEMIS E observe bursty bulk flows and dipolarizations (Kepko et al., 2009) as they orbit from the premidnight to midnight sector plasma sheet and through the magnetic equator, as depicted in Figure 1. While observing the fast flows, THEMIS D is at $x_{GSE} \sim -11.1\ R_E$ and THEMIS E at $x_{GSE} \sim -10.6\ R_E$. ($L \sim 12$, geomagnetic latitude about 7.2°.) In the midst of an overall trajectory crossing the magnetic equator from positive to negative geomagnetic latitudes, THEMIS skims the magnetotail geomagnetic equator between ~ 05:25 UT and 05: 40 UT. During this interval, THEMIS D and E detect strong earthward ion flows as high as over 400 km/s, accompanied by strong magnetic fluctuations, magnetic dipolarizations, electron density and temperature dropouts, and scattering of electrons to higher energies and out of the plasma sheet (as shown for THEMIS D, in Figure 2). Electron pitch angle

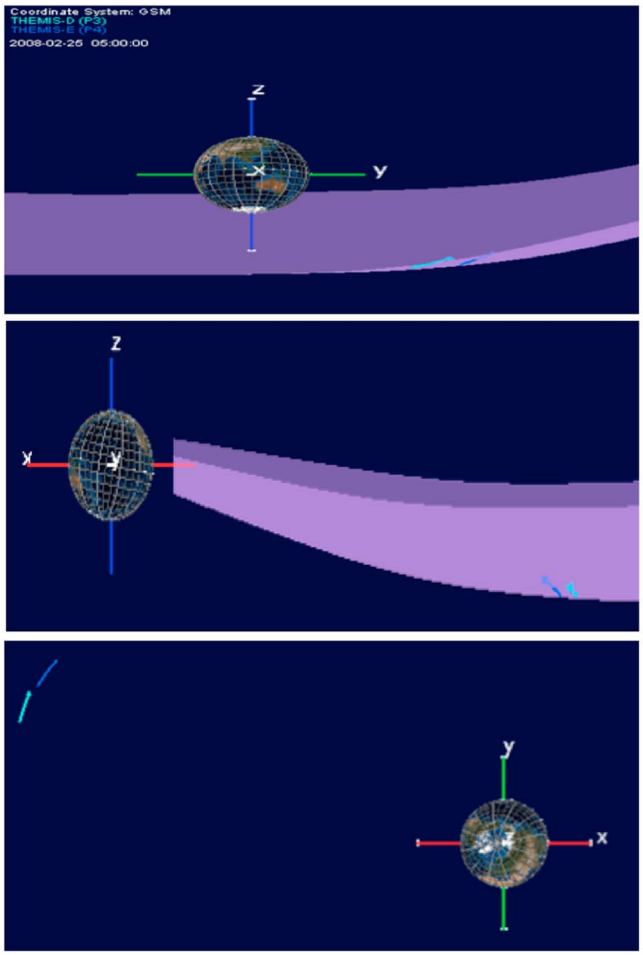

Figure 1. The orbits of THEMIS D (cyan) and THEMIS E (blue) between 05:00 and 06:00 UT in GSM coordinates. The purple surface in the *yz* and *xz* views is a model-based representation of the neutral sheet. The spacecraft start out above the neutral sheet and by about 05:40 UT have passed through it. THEMIS = Time History of Events and Macroscale Interactions during Substorms.

distributions are field aligned in the parallel and antiparallel directions at various points during the interval, especially pronounced at the fast flow onset. Kepko et al. (2009) establish a connection between the fast flows and substorm auroral forms. They report that the all-sky imager at Gillam, Canada, detects an equatorward moving diffuse aurora leading to onset about 90 s after the THEMIS probes observe the fast flows. A discrete aurora just westward and equatorward of the diffuse aurora indicates the development of a substorm current wedge.

For our wave data analysis, we use THEMIS D and E electric waveform (electric field instrument, EFI), magnetic search coil waveform (SCM), and Filterbank (FBK) electric and magnetic field spectral data during the interval of intense earthward particle flows from about 05:25 to 05:40 UT. The EFI and SCM instruments collect wave burst resolution data gathered over ~ 15 s at 0.125 ms (8.192 kHz) cadence and particle burst resolution data gathered over ~ 12 min at 8 ms (128 Hz) cadence. THEMIS D and E fields instruments are in wave burst mode for a brief time interval starting around 05:29:19 and 05:35:57 UT, respectively, while they are in particle burst mode for the entire fast flow interval. The FBK data are available for a longer duration before, during, and after the fast flow observation, and for our interval provide slow-survey time-frequency spectra in six logarithmically spaced frequency bands between 1.26 and 5994 kHz. Not only do FBK spectra have limited frequency resolution, but because they are computed on board for extended periods, they also have lower time resolution through windowing. Calibrated electron and ion moments and distributions are available from the Electrostatic Analyzer (ESA) instrument at a 3-s spin cadence. Unless otherwise specified, all vector data are in despun spacecraft DSL coordinates which are approximately equivalent to the GSE system.

We perform minimum variance, Faraday residue, and spectral analysis—including a wavelet-based singular value decomposition (SVD)—of electric and magnetic wave burst data to identify electrostatic and electromagnetic waves and their properties. In addition to a standard spectral analysis to derive the frequency and dispersive properties of the waves, we use a SVD based on complex-valued wavelets to estimate the polarization and propagation direction of the waves across the time-frequency domain. To supplement the latter method, we also apply a minimum variance analysis (MVA), based on magnetic field data, and the method of Faraday residues (FR), using both electric and magnetic field data, to estimate the direction of propagation, or wave normal angle, θ_N. Because we must also consider Doppler shifting within the fast flows, we use the estimated direction of wave propagation to find the cosine of the angle between the ion velocity $\mathbf{v}_i$ and the wave vector direction $\mathbf{k}/|\mathbf{k}|$to derive the extent of frequency shifting for a given wave mode. Since we are restricted to single spacecraft data, multispacecraft methods such as *k* filtering are not feasible.

We apply the wavelet algorithm proposed by Park et al. (1987) and Lilly and Park (1995) in the study of seismic waves to analyze the time-frequency spectra and the wave polarization. The method yields the propagation direction as a byproduct, under the assumption that the wave polarization is either parallel or perpendicular to the direction of propagation. In its use, we assume the waves are either perpendicularly polarized plane waves for electromagnetic waves or parallel polarized for electrostatic waves. Park et al. (1987) and Lilly and Park (1995) designed the time and frequency dependent wavelet windows, whose spectra are computed by a discrete Fourier transform, as multitapers that reduce bias and minimize spectral leakage. At each frequency band, the method combines a number of orthogonal wavelets, yielding the same low variance, leakage minimization properties as multitapers (Thomson, 1982; Thomson, 1990). The wavelets' properties parallel those of prolate spheroidal series. At the same time, forming complex

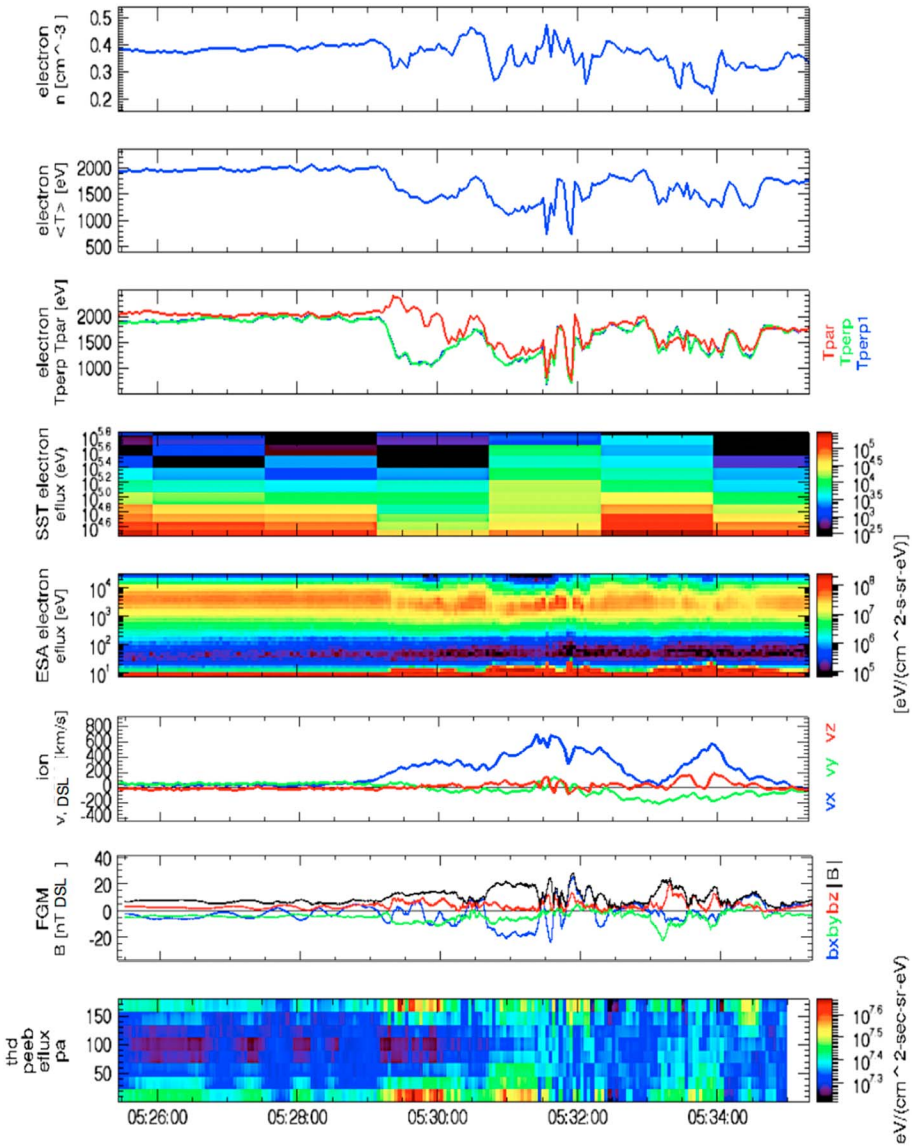

Figure 2. An overview of the bursty bulk flow measurements on 25 February 2008 from THEMIS D, as reported by Kepko et al. (2009). (top to bottom) Electron density, average electron temperature, electron perpendicular and parallel temperatures, SST electron energy flux, ESA electron energy flux, ion bulk velocity, magnetic field components and magnitude, and electron pitch angle distributions (all vector data are in DSL ~ GSE). ESA = Electrostatic Analyzer; SST = Solid State Telescope.

wavelets by pairing alternating even and odd wavelets retains the phase information necessary to capture both the type and sense of wave polarization across the time and frequency domain, for example, linear or elliptical, right- or left-handed, polarization. Furthermore, a SVD of the wavelet spectral decomposition yields the direction of polarization of the wave components with respect to the background coordinate system. The first three eigenvalues and corresponding eigenvectors estimate the directions of maximum, intermediate, and minimum wave variance. The first eigenvalue captures the strongest motion, the second the intermediate, and the third the minimum. Hence, one can also estimate the direction of propagation if one assumes, for example, a plane wave, where the direction of minimum *disturbance*, or the eigenvector belonging to the third eigenvalue, approximates the direction of propagation. We refer the reader to Park et al. (1987) and Lilly and Park (1995) for further details on the technique.

Two alternative methods for deriving the wave normal from single spacecraft measurements are the FR method and the MVA. These methods are, however, limited to the entire time and frequency range of the

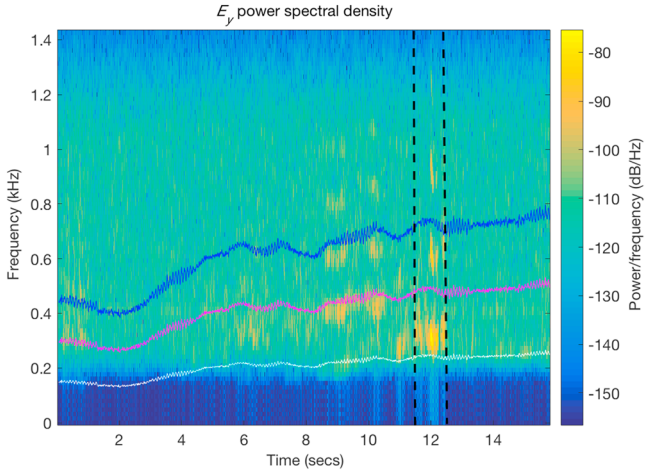

Figure 3. One perpendicular component of the THEMIS E EFI wave burst-rate spectra, filtered below the fundamental electron cyclotron frequency, for the wave burst interval in seconds following 05:35:46.365. The first two cyclotron harmonics are plotted as a function of time in purple and blue. The spectral bands appearing near and between the cyclotron harmonics are evidence of ECH waves. The dashed lines delimit the interval analyzed in Figure 4. EFI = electric field instrument; ECH = electron cyclotron harmonic.

signal of interest. The FR method exploits both the electric and magnetic fields and integrates Faraday's and Gauss's laws into an optimization algorithm (Khrabov & Sonnerup, 1998; Terasawa et al., 1996). As a dividend, this method also provides the velocity of the medium along the direction of propagation. It extends the MVA analysis (which executes a minimization based on Gauss's law, (Sonnerup & Cahill, 1967)) to include the minimization of the residue of Faraday's law. The method combines Gauss's and Faraday's laws into a single minimization function, which Khrabov and Sonnerup (1998) cast in the form of an eigenvalue decomposition. The wave speed along the normal direction is then given by $\frac{\delta\mathbf{E}\times\delta\mathbf{B}}{|\delta\mathbf{B}|^2}\cdot\hat{\mathbf{n}}$, where $\delta\mathbf{E}$ and $\delta\mathbf{B}$ are the electric and magnetic fluctuations, and $\hat{\mathbf{n}}$ is the direction of propagation. Unlike the wavelet SVD, the method incorporates all times and frequencies during the wave interval. Therefore, we first filter the data to the frequencies of interest before applying the method.

We use electron distributions and wave spectral parameters to elucidate the nature—that is, free energy source, wave growth, and wave-particle scattering—of the wave-particle interactions that lead to diffuse aurora precipitation. Electron distributions indicate the free energy source, and given features of the latter, we use a previous analysis of oblique whistler growth rates for similar physical conditions. From the wave spectral amplitudes identified in the wave burst resolution data, we determine their efficiency in scattering electrons out of the plasma sheet by feeding the wave power, mean and bandwidth frequencies, and average background plasma density and magnetic field strength, into a wave diffusion analysis. Here we have numerically derived the scattering diffusion coefficients $D_{\alpha\alpha}$ for both whistler and ECH waves, as discussed in Tripathi and Singhal (2009), Tripathi et al. (2013), and Tripathi et al. (2017). To compare with other works on whistler waves near magnetic holes and flux pileup regions (such as Khotyaintsev et al., 2011; Santolik, 2008; Tsurutani et al., 2009; Zhima et al., 2015), we inspect the placement of the whistlers with respect to dipolarization fronts and flux pileup regions.

Because the wave burst resolution data are limited to very short intervals, on the order of 15 s, we supplement the wave burst data with fields at particle burst resolution. These longer intervals reveal patterns of occurrences of electrostatic and electromagnetic waves and their frequency dependence. The FBK spectra provide yet longer time intervals by which we infer or limit the possible wave modes as well as their correlation with location and other activity in the magnetotail.

3. Analysis

THEMIS wave burst electric field spectra have frequency bands consistent with ECH waves, as demonstrated in Figure 3. Figure 3 displas the E_y component (though **B** points along all three axes, it points predominantly in the x and z directions). The spectra are derived from EFI data after filtering between the minimum f_{ce} and $4f_{ce}$, where f_{ce} is the electron cyclotron frequency $\omega_{ce}/(2\pi) = eB/(2\pi m_e)$. In Figure 3, the time axis is in seconds after 05:35:46.365 and the colored lines correspond to ω_{ce} and its two higher harmonics. Because the nondispersive modes lie near or between these cyclotron harmonics and because they are electrostatic, we conclude these are ECH waves. The top panel of Figure 4 displays the wavelet spectrum of one of the transverse components of the ECH waves after 05:35:57.83. The wave data have been rotated into a coordinate system where the first two orthogonal components (new x and y) lie in the plane perpendicular to the background magnetic field, and the third (new z) component lies parallel to the background field. Here we show the spectra of only the perpendicular components because they are the least noisy. Though there is a small parallel component at a few locations, it is only at most 18.5% of the transverse spectral energy at the same locations. The bottom panel is the map of the wave normal angle θ_N in the time-frequency domain, overlaid with the contours of the wave spectrum (in red) to pick out the region of interest. The value of θ_N from the SVD method ranges from about 80° to just over 90° in the regions of peak spectral

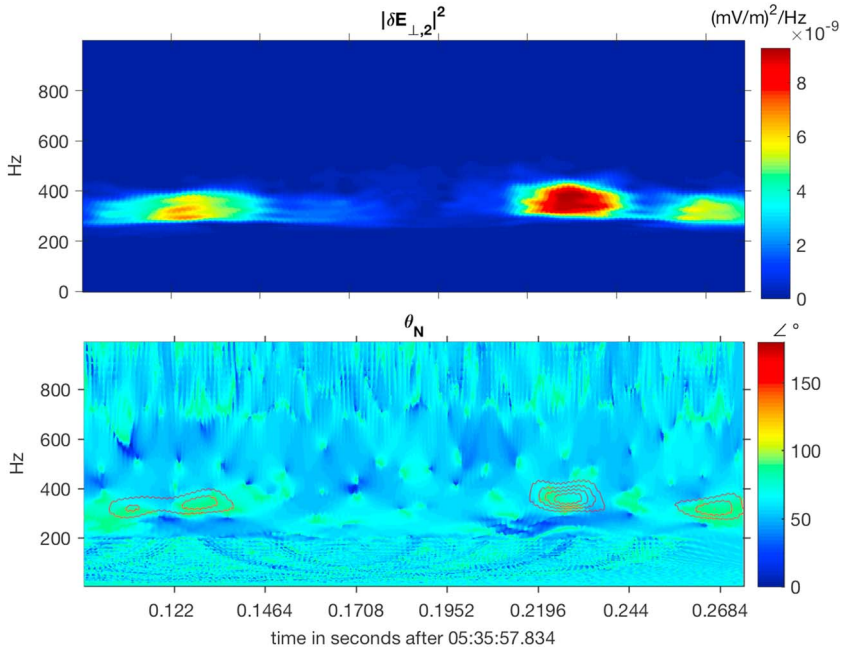

Figure 4. (top) The wavelet spectrum for the first harmonic of the ECH waves observed by THEMIS E in burst mode during the fast flow interval between dashed lines in Figure 3. (bottom) The corresponding wave normal angle in the time-frequency domain as calculated through the wavelet SVD. The red contours represent the peaks of the spectrum and therefore the region of significance of the angle calculations. SVD = singular value decomposition.

energy, denoted by red curves in the bottom panel of Figure 4. This further corroborates the identification of ECH waves. For the purposes of calculating the diffusion coefficients $D_{\alpha\alpha}$, the mean electron density is n_e ~ 0.4/cm^3 and the mean magnetic field magnitude is$|B|$~ 18.77 nT. We find that $D_{\alpha\alpha}$ for the ECH waves ~ 9.6*10^{-10} (mV/m)^2/Hz. For details on the calculation of $D_{\alpha\alpha}$, we refer the reader to Tripathi and Singhal (2009), Tripathi et al. (2013), and Tripathi et al. (2017). We do not observe electromagnetic or whistler waves during this short interval. THEMIS D also observes a possible weak signature of ECH waves during its wave burst interval, but the signal-to-noise ratio is too weak for a robust analysis.

For an approximately 9 s wave burst data acquisition following 05:29:19.618 UT, THEMIS D observes a series of dispersive waves below the electron cyclotron frequency f_{ce} ~ 340 Hz and above the ion cyclotron frequency (f_{ci} < 1 Hz). We are in a regime with $\omega_{pe}/\omega_{ce} >> 1$, $\omega_{ci} < \omega < \omega_{ce}$, and $c/v > 1$, where ω_{pe} is the plasma frequency, c is the speed of light, and v is the wave phase speed, making whistlers a candidate for electromagnetic emissions. Figures 5 and 6 present the physical parameters underpinning the essential physics behind the formation of the whistler waves in this region, which we will discuss in more depth in the conclusions. In Figure 5, the shaded interval begins with the dipolarization and includes the flux pileup region, and the interval between dashed lines is the section of wave burst data that we analyze in more detail. Figure 6 magnifies the interval following the dipolarization, and relates the earthward bulk flow and the flux pileup to the electron temperature anisotropy, as discussed later in detail. The third panel of Figure 5 shows the DSL coordinate system flux-gate magnetometer (FGM) B_x and B_z components for the entire bursty bulk flow observation. The fourth panel is the SCM wave burst interval starting at about 05:29:36.225 that falls between the dashed lines in the panel above. The white line over the spectral plot corresponds to f_{ce}. The waves' rising tone is typical of whistler chorus frequently observed near the magnetic equator and, in the inner magnetosphere, is associated with hiss (Helliwell et al., 1986)—although here we do not observe hiss in either the magnetic or electric field spectra. The periodicity of the bursts is about 0.2 to 0.4 s, as observed previously for chorus waves (Helliwell, 1965; Tagirov et al., 1999). A similar dispersion in the electric field data between the ion and electron cyclotron frequency suggests that these are whistler waves Figure 6.

An in-depth analysis of spectral properties of one of the wave bursts confirms that these are indeed whistler waves but propagating highly obliquely to the background magnetic field. Figure 7 displays a wave emission

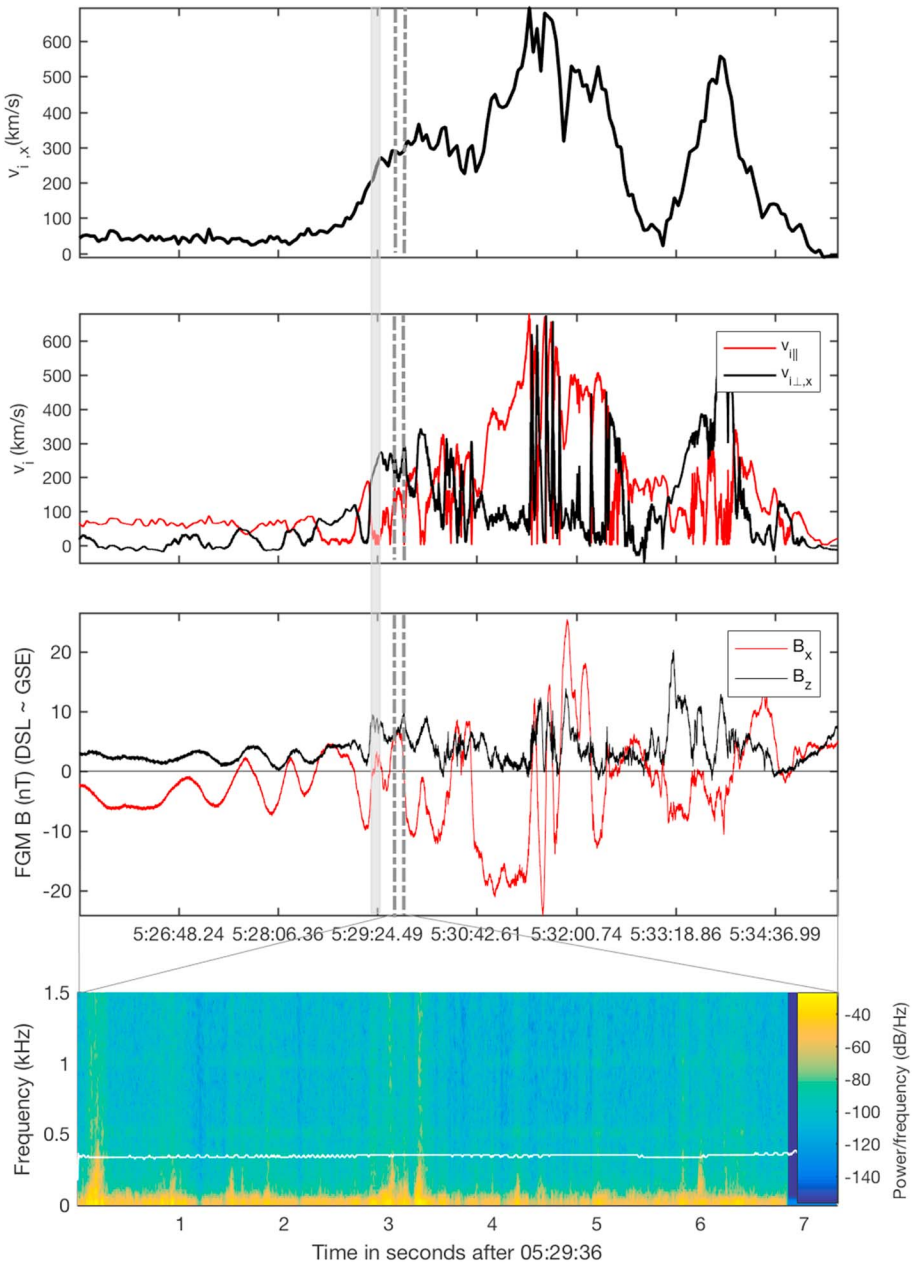

Figure 5. The *x* component of the THEMIS D ion velocity (first panel), the perpendicular (black) and parallel (red) components of the ion velocity (second panel), B_x and B_z (third panel), and the magnetic field power spectral density for the interval between dashed lines above (fourth panel). The shaded interval starts with the dipolarization and includes the flux pileup region. The spectrum is consistent with chorus whistler waves with a periodicity of 0.2–0.4 s.

over an interval less than 1 s starting at about 05:29:36.23. The top four plots are the component and total power spectral density of magnetic and electric emission, where the components are rotated into field-aligned coordinates. The bottom two plots are the time-frequency spectrum of the wave normal angle θ_N estimated from the SVD of the magnetic and electric field wavelet transforms, respectively. The white contours superposed on the angle spectrum delineate the regions of peak spectral energy in the waves.

The perpendicular spectra show demarcation of the lower band component from the upper band component that arrives later. Though the peak spectral power of the upper band exceeds that of the lower band, because the duration of the lower band emission is longer, the total power it delivers is greater. Despite the more oblique propagation angle of the lower band, as we discuss below, the parallel component of the lower band

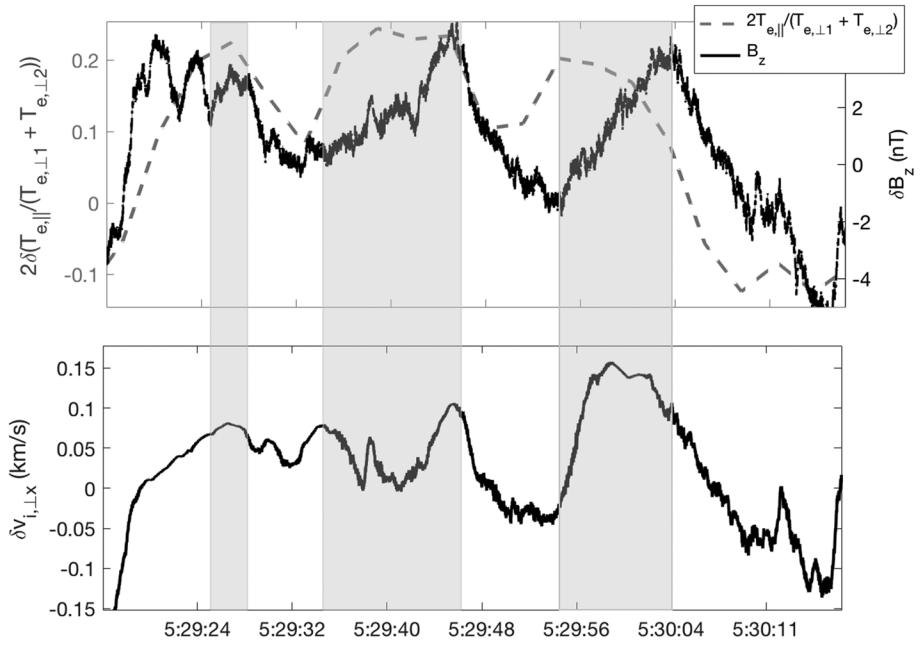

Figure 6. The fluctuations of the background B_z and of the electron temperature anisotropy $2T_{e,||}/(T_{e,\perp 1} + T_{e,\perp 2})$ (top) and of the earthward perpendicular plasma velocity $v_{ix,\perp}$ (bottom) following the first dipolarization front at 5:29:19 (see Figure 5). (The fluctuations are calculated by subtracting the mean over the interval.) The shaded intervals pick out where the combination of $v_{ix,\perp}$ and B_z are expected to favor Fermi acceleration over betatron acceleration. The second shaded interval corresponds to the THEMIS D wave burst interval in the fourth panel of Figure 5.

contribution is much weaker than that of the upper band. We will show that this feature reflects a difference in the ellipticity of the wave polarization of the two frequency bands.

At the peak value of the lower band, the magnetic field SVD gives a propagation angle $\theta_N \sim 63°$, and at the peak of the upper band, a somewhat smaller angle of 46°. This is in general agreement with the results of the MVA, which gives $\theta_N \sim 52° \pm 4°$ for the lower band (the waves are first band-pass filtered to the desired frequency range). The FR method gives 70° for the lower band, and between 36° and 58° for the upper band, depending on the length of the interval used. Because the methods are all unique only up to a sign, the angles could represent propagation either parallel or antiparallel to B_0. Like the FR method, the electric field SVD yields a larger value for θ_N than the magnetic field SVD, because, unlike $\delta\mathbf{B}$, it has a component along B_0, assuming that the polarization is perpendicular to the direction of propagation. The ratios of the spectral components show that $\delta E_{||}/\delta E\,(\sim 0.66) > \delta B_{||}/\delta B\,(\sim 0.13)$ for the upper band chorus, implying an electrostatic component along B_0. Because for oblique propagation there is an electrostatic component along the field, one should not base an estimate of θ_N on the electric field (Bellan, 2013). This parallel electrostatic component has been observed in oblique whistler chorus previously, where it was also found to increase in the upper tones (Inan & Bell, 1991; Mourenas et al., 2015; Santolik et al., 2009; Tripathi et al., 2017; Zhang et al., 1993). The oblique propagation angle explains why there is a fluctuating magnetic wave component along the background magnetic field. The angles of propagation from the magnetic field SVD analysis are below the resonance cone θ_r ($\theta_r \sim \cos^{-1}(\omega/\omega_{c,e}) \sim 81°$ for the lower band and 75° for the upper band) and approaching the Gendrin angle θ_G ($\theta_G = \cos^{-1}(2\omega/\omega_{c,e}) \sim 73°$ for the lower band and 58° for the upper band). At the Gendrin angle, the wave achieves its highest phase velocity parallel to B_0, which decreases for angles above that, going down to 0 at θ_r (Gendrin, 1961). The Gendrin mode is nondispersive, and its group velocity is parallel to B_0 (Verkhoglyadova & Tsurutani, 2009). Gendrin waves therefore travel close to the direction of the resonant electron guiding center velocity (Santolik et al., 2009). We note that the lower band chorus observed in this interval shares many features with the Gendrin mode.

Because the waves are detected within fast plasma flows, we must consider the possibility the waves are Doppler shifted in the spacecraft frame. Using the minimum variance estimate of the propagation

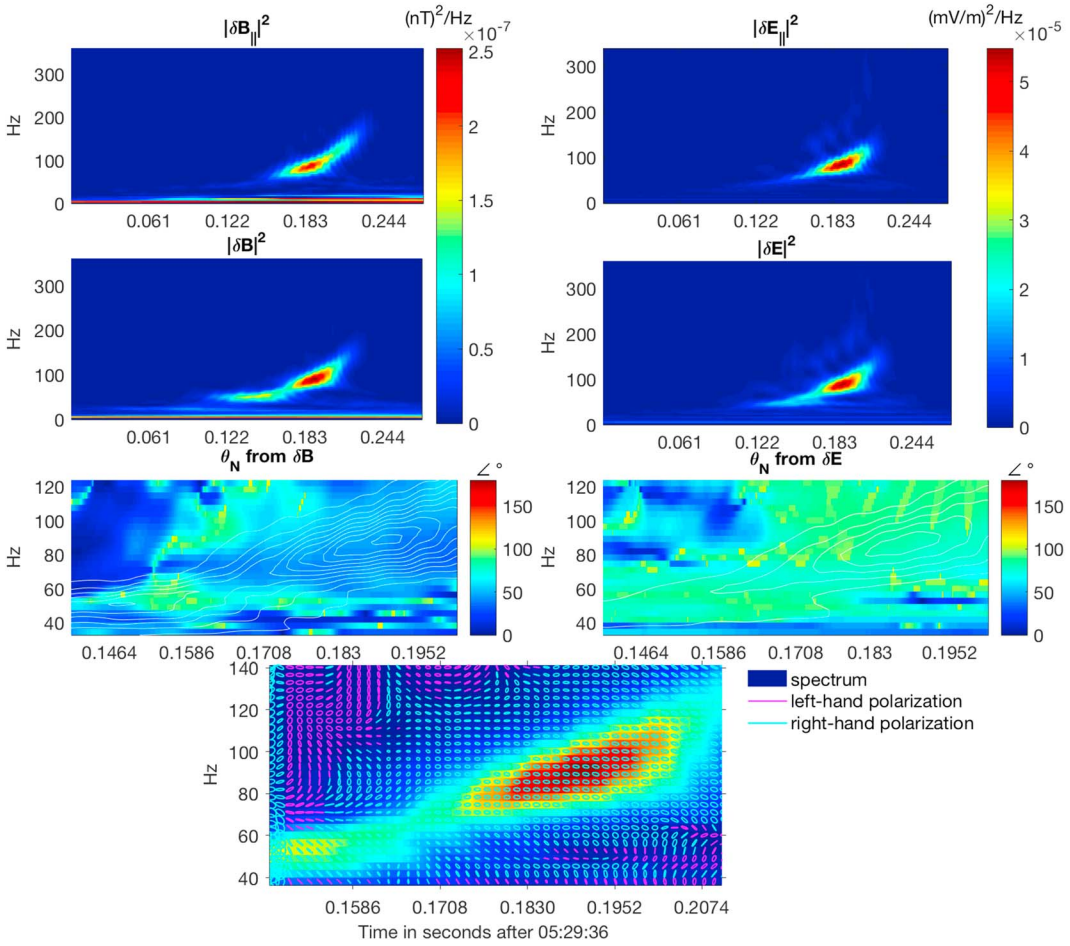

Figure 7. (top two rows) The parallel and total magnetic field spectra (left) and parallel and total electric field spectra (right) for the strongest whistler observed during the THEMIS D wave burst interval. (third row) The wave normal angles determined from the wavelet SVD analysis from magnetic (left) and electric (right) fields. The superposed white contours represent the spectra of the upper and lower band chorus emissions from above, and hence where the angle calculations are significant. (bottom row) The results of the wavelet polarization analysis are represented by blue and purple curves superposed over the spectrum, the color depending on the sense of polarization with respect to the wave normal direction k. The curves are projections of the polarization in a plane perpendicular to k. The circles reveal left-hand circularly polarized waves. The polarization analysis is meaningful where the spectrum is strong.

direction in the whistler dispersion relation gives an upper bound on the degree of Doppler shifting from $\omega_p = \omega_{sc} - \mathbf{k}\cdot\mathbf{v}$, where ω_p is the frequency in the plasma frame, ω_{sc} is the frequency in the spacecraft frame, and $\mathbf{v}$ is the plasma velocity. We use the ion velocity, because we believe the electron velocity moments undergo aliasing from the frequent magnetic field changes. Because v_i is less than the Alfvén speed $v_A \sim 450$ km/s, we cannot assume the Taylor frozen-in approximation. Assuming a whistler mode, the worst-case shift would occur for $\mathbf{k} = \omega_{ce}/v$ and $\mathbf{k}||\mathbf{v}_i$. Because we find that the wave phase speed $v \cong \frac{\delta\mathbf{E}\times\delta\mathbf{B}}{|\delta\mathbf{B}|^2}\cdot\hat{\mathbf{n}}$ derived from the FR method is highly variable with time interval and frequency band, we believe a more reliable estimate of the wave speed is found from fitting the oblique whistler dispersion relation

$$\omega = \frac{\omega_{ce}k^2c^2\cos(\theta_N)}{k^2c^2 + \omega_{pe}^2} \tag{1}$$

to the spectral data. From the fit, we find $v \sim 5\times10^3$ km/s, where we have used the SVD value of $\theta_N = 63°$ for the lower band and $\theta_N = 46°$ for the upper band. Given the range of observed emission frequencies $f \sim 20$–180 Hz and $k \sim 2\pi f/v$ with $v \sim 5\times10^3$ km/s, the dispersion relation is consistent with the range $(0.1–0.8)f_{c,e}\cos(\theta_N)$ of lower and upper band chorus. For the observed frequencies between $f \sim 20$–180 Hz, the factor

$k^2c^2/(k^2c^2 + \omega_{pe}{}^2)$ in (1) ranges from 0.1 to 0.8. Lower band frequencies (0.1–0.5)$f_{c,e}\cos(\theta_N)$ ~ 23 to 75 Hz for $\theta_N = 63°$, which agrees well with the observations. Upper band frequencies range between (0.5–0.8)$f_{c,e}\cos(\theta_N)$ ~ 115 to 183 for $\theta_N = 46°$. While the upper limit of this range agrees well with the measured upper band frequency, the lower limit is about 20 to 30 Hz higher. We believe that we can attribute the difference, at least in part, to the fact that θ_N varies over the spectrum in Figure 5, taking on higher values up to roughly 55 to 60° on the lower and outer edges of the spectral peak. With $\theta_N = 60°$, f ~ 80 Hz, and we retrieve a better match between the theoretical lower limit and the data. Using $v \sim 5 \times 10^3$ km/s, f_{ce} ~ 340 Hz, and $v_i \cong 176$ km/s, the worst-case Doppler shift is only about 3 Hz. Therefore, we can safely believe the waves lie in the whistler frequency range.

The waves are circularly polarized, with a high degree of ellipticity in the lower band wave. The bottom panel of Figure 7 captures the time and frequency-dependent polarization of the magnetic field data that we have rotated into wave vector-aligned coordinates, where the wave vector points out of the page. The polarization for each time-frequency bin is captured by a curve that depicts the form of the wave motion in a given plane. When labeled *transverse 1 - transverse 2*, for example, the polarization curves placed over the spectrum represent the wave motion in the plane perpendicular to **k**. For the analysis, we have chosen the **k** direction derived from the SVD at the peak of the upper band spectrum (and, therefore, the projections perpendicular to **k** well be less accurate for the lower band emissions than for the upper band emissions). Polarization curves that are lines indicate linear polarization in the plane; curves that are circular or elliptical likewise indicate circularly or elliptically polarized wave motion. If a curve is tilted, this captures the projection of the polarization curve onto the plane.

Since the methods to calculate wave normal angles yield estimates unique only up to a sign, whether propagation lies parallel or antiparallel to the background field remains ambiguous. For antiparallel propagation, the waves are right-hand polarized with respect to **B**, as expected for a whistler. At the time THEMIS D observes this whistler, $B_{0,x}$ is briefly positive (see Figure 5), indicating THEMIS is temporarily above the magnetic equator. Thus, this observation is consistent with the statistical likelihood noted by Santolik et al. (2009) for oblique whistler chorus to propagate in a sense antiparallel to B_0 at negative geomagnetic latitudes and in a sense parallel to B_0 at positive geomagnetic latitudes.

Verkhoglyadova and Tsurutani (2009) and Bellan (2013) demonstrate that, under highly oblique propagation, a whistler waves' magnetic component retains its (right-hand) circular polarization with respect to **k**. Here we also note that the upper band polarization is more circular than the lower band polarization. This is aside from the fact that the projection of the lower band wave polarization is less accurate (and thus appears less elliptical) than that of the upper band because we have used the upper band **k** for the whole time-frequency domain. In the lower band chorus, the amplitude of δB along the parallel and one of the perpendicular directions is much smaller than along the other perpendicular direction. Thus, the rotational polarization is highly elliptical and less circular. This also explains why the lower band spectral power parallel to **B** is much smaller than that of the upper band power, even though the lower band wave is more oblique. As a check for consistency, in Figure 8 we show that the time evolution of the magnetic field wave components in a coordinate system aligned with the background magnetic field (the new z direction) also yields a right-hand polarized wave. Thus, for oblique propagation in a sense parallel to **B**, the wave is right-hand polarized with respect to both **B** and **k**, as expected. Figure 8 includes the electric field, but its polarization in the magnetic field-aligned coordinate system is not so transparent, since it has a component along **B**.

Parallel electron beams provide the local free-energy source for the whistler waves. $T_\perp/T_{||} < 1$ throughout the burst interval, precluding electron temperature anisotropy as the energy reservoir. Also, electron temperature anisotropy $T_\perp/T_{||} > 1$ preferentially produces wave growth at parallel propagation. Helliwell et al. (1986) discover that magnetospheric hiss signals can, through second-order cyclotron resonance, convert into coherent chorus emissions. However, we do not observe hiss in the high-resolution data, and we argue that the low-resolution data we present later give the illusion of hiss from time aliasing of the very fast coherent whistler signals. Nor do we find a nonlinear instability, since $\delta B_0/B_0 << 1$. Therefore, we argue that parallel electron beams are the source for the oblique whistlers.

If we look at the electron distributions for the time interval in Figure 7, we can see that there are parallel electron beams with anisotropic temperature, and that the large electron $T_{||}$owes, to some extent, to the

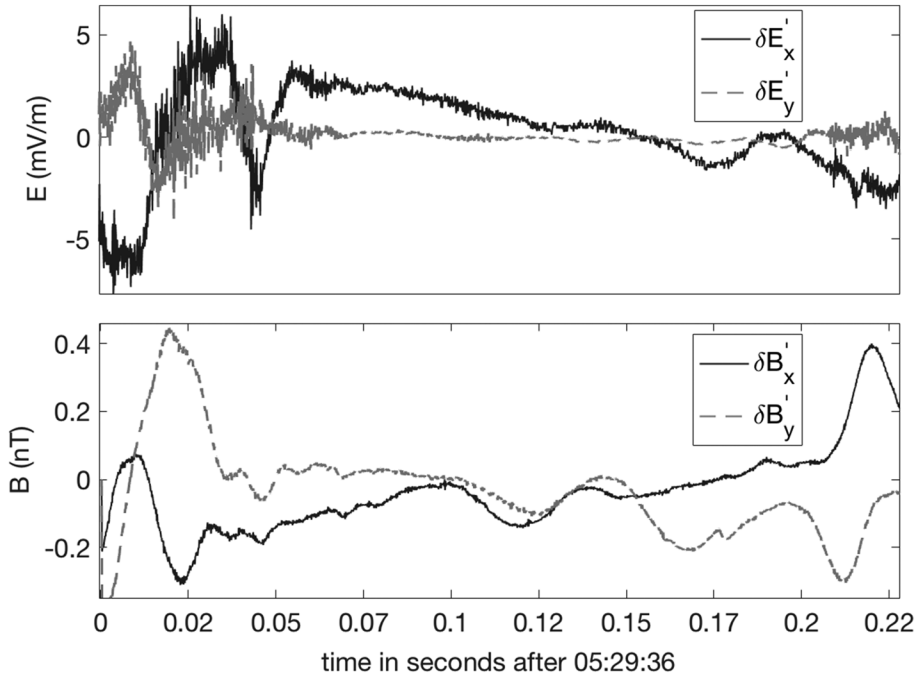

Figure 8. The perpendicular components of the wave electric field (top) and of the wave magnetic field (bottom) of the THEMIS D whistler wave in Figure 7, in a coordinate system aligned with the magnetic field. The time interval is the same as that in Figure 7.

parallel beams. Figure 9 shows the electron distributions from the spins before, during, and after the whistler observation of Figure 7. The left and right columns show distributions in the xz and yz planes, respectively, where z is along the background magnetic field. The distribution in the circular inset is from the period before the dipolarization and fast flows, revealing temperature anisotropy without any clear evidence of beams. The beams seem to be unique to the fast flows. The whistler in Figure 7 occurs during the 5:29:34 to 5:29:37 spin. There are some whistlers that fall within the spins following this one, as well. (We do not know about whether there are whistlers preceding 5:29:34, because the wave burst data are not available then). There are a number of beams parallel to B_0, ranging from a few hundred electron volts to over 2 keV ($v_e \sim 1 \times 10^4$ to 3×10^4 km/s). The beams at or below 1 keV and all the beams in 5:29:34 to 5:29:37 have positive anisotropy, namely, they are hotter in the perpendicular direction than in the parallel direction. The beams above 2 keV have negative anisotropy. Though there is a slower antiparallel beam during a few spins, most—and especially the most energetic—beams are parallel to B_0. During the 3-s spin that encompasses the time interval of the waves in Figure 7 (third panel from top, Figure 9), the beams have become more parallel and more diffuse in energy. The higher-energy beams reappear in the spins following this one. This time evolution is consistent with the electron beams gaining and losing energy episodically. This implies that the waves also propagate parallel and antiparallel to the electron beams.

The two possible resonances between the electron beams and the whistler waves are the Landau and cyclotron resonances. Landau resonance occurs for $v_{e,||} = v_{||}$, where $v_{e,||}$ is the electron speed parallel to B_0, and $v_{||}$is the wave phase speed parallel to B_0. The first-order nonrelativistic cyclotron resonance condition is $=\omega_{ce} - \mathbf{k} \cdot \mathbf{v}_{e,||}$, where $k_{||}$is the wave vector component parallel to B_0. In one-dimensional numerical simulations of hot, anisotropic electron beams in a cold, magnetized plasma, Zhang et al. (1993) find that the beams excite an electrostatic component parallel to B_0 that Landau resonates and an oblique whistler wave that undergoes first-order cyclotron resonance. They find positive whistler growth rates at oblique angles, including a peak whistler magnetic wave intensity at $\theta_N = 20°$ and $\theta_N = 45°$. Mourenas et al. (2015) demonstrate that Landau and cyclotron resonances with low-energy parallel electron beams generate oblique whistlers—though their analysis is concerned with waves propagating above the Gendrin angle and just below

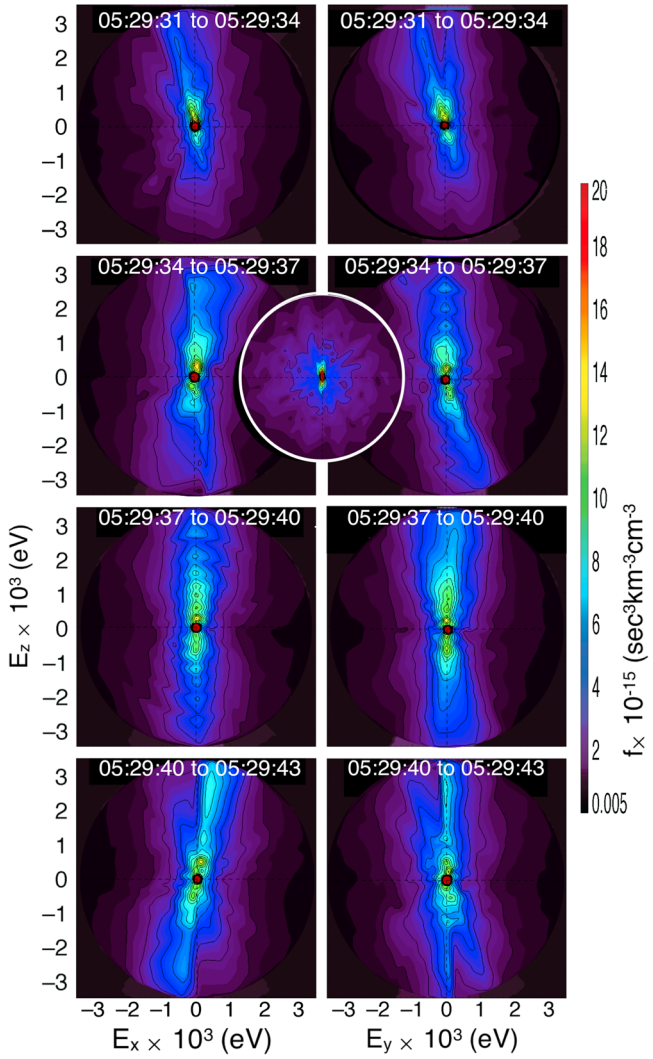

Figure 9. Electron energy phase-space distributions for the interval right before, during, and after the intense THEMIS D whistler observation of Figure 5, with time progression from top to bottom. The whistler observation of Figure 7 lies within the time window 5:29:34 to 5:29:37. The vertical z axis is along the magnetic field direction, and the y axis is along the projection of the GSM y direction. The left panel shows distributions in the x-z plane and the right panel in the y-z plane. The circular inset between the columns in the second row shows a distribution from 5:27:31 to 5:27:34, before the onset of the fast flows and the whistler chorus. It is not to scale: its purpose is to show the comparatively smooth distributions before the onset of fast flows.

the resonance cone. Using the dispersion relation given by (1), the Landau resonant condition $v_{e,||} = v_{||}$ yields the electron resonant energy

$$E_{||,lr}(\mathrm{keV}) = \frac{250\omega_{ce}^2\omega\left(\cos(\theta_N) - \frac{\omega}{\omega_{ce}}\right)}{\omega_{pe}^2\omega\cos^2(\theta_N)} \quad (2)$$

and the cyclotron resonance condition yields the resonant electron energy

$$E_{||,cr}(\mathrm{keV}) = \frac{250(\omega - \omega_{ce})^2(\omega_{ce}\cos(\theta_N))}{\omega_{pe}^2\omega\cos^2(\theta_N)}. \quad (3)$$

For parameters close to those of the present data, Sauer and Sydora (2010) calculate oblique whistler growth rates from cyclotron resonance of cold parallel electron beams. Their results predict positive electron cyclotron resonance whistler growth rates at $\omega \sim 0.3\omega_{ce}$, $kc/\omega_{pe} \sim 1$, $\theta_N \sim 45°$, and $v_{b,e}/v_{A,e} = 2$ (their Figure 3). Others, for example, Kaur and Pandy (2017), Pandey and Misra (2002), Zhang et al. (1993), have performed electron beam-whistler instability analyses for somewhat different conditions. Zhang et al. (1993) investigates for hot electron beams. Assuming a beam-to-background electron density ratio $n_{e,b}/n_{0,e} = 0.01$, parallel electron beam energies $v_{b,e} \geq 1.5v_{A,e}$, and electron $\beta_e < 0.01$, the Sauer and Sydora (2010) calculations at $\theta_N = 50$, 60, and 70° give positive whistler growth rates. (Though they acknowledge the viability of the Landau-Cerenkov resonance mechanism for beam velocities $<0.5v_{A,e}$, they limit their calculations to beam velocities $\geq 1.5v_{A,e}$ and thus to electron cyclotron resonances.) They find positive growth rates at $v_{b,e} > 1.5v_{A,e}$ for oblique θ_N more generally, with θ_N increasing for higher beam velocities. The growth rates are positive for oblique angles where $0.5 \leq kc/\omega_{pe} \leq 2$, with kc/ω_{pe} increasing nonlinearly with θ_N. They find that fluid and kinetic descriptions give nearly identical results for $\beta_e < 0.2$. The important point here is that Sauer and Sydora (2010) find that, for a cold plasma, the cyclotron resonant growth rates monotonically increase for increasing θ_N up to about $\theta_N \sim 60°$ for 2-keV electron beams (and up to even larger angles for higher beam energies). Therefore, the resonance necessary to produce whistler waves from electron beams is more likely for oblique wave normal angles.

In our data, $\beta_e \sim 1.5$, $n_{e,b}/n_{0,e} \sim 0.005$–$0.01$, and $0.77 \leq v_{b,e}/v_{A,e} \leq 1.65$, $kc/\omega_{pe} \sim 0.61$ for the lower band chorus, and $kc/\omega_{pe} \sim 1.2$ for the upper band chorus. Thermal effects will influence our results, since $\beta_e > 0.2$. Thus, the relevant plasma parameters in our data lie very close to those of the Sauer and Sydora (2010) simulated data for the observed beam energies that exceed $\sim 1.5v_{A,e}$. For the upper band chorus that we observe with $\theta_N \sim 46°$, $\omega \sim 0.3\omega_{ce}$, and $kc/\omega_{pe} \sim 1.2$, the beam energies with $v_{b,e}/v_{A,e} > 1.5$ extrapolate to a curve very close to the curve corresponding to $v_{b,e}/v_{A,e} = 2$ in Figure 3 of Sauer and Sydora (2010). (We omit discussion of the lower band chorus observations here since they are only unstable to Landau/Cerenkov resonance, which is not examined in the Sauer & Sydora, 2010 work). However, given that $\beta_e \sim 1.5$, we should consider thermal effects. In the cold plasma approximation, Sauer and Sydora (2010) find that Landau damping overwhelms any potential wave growth from cyclotron resonance when $\beta_e > 0.2$. Zhang et al. (1993) and Mourenas et al. (2015) point out that in order for the whistler waves to be excited by hot electron beams, the beam must have temperature anisotropy $T_{e,\perp}/T_{e,||} > 1$.

Figure 10 plots the curves for $E_{||,lr}$ and $E_{||,cr}$ as a function of frequency f in Hertz for both the upper and lower band waves. For the lower band waves, we have used $\theta_N = 63°$, and for the upper band waves we have used

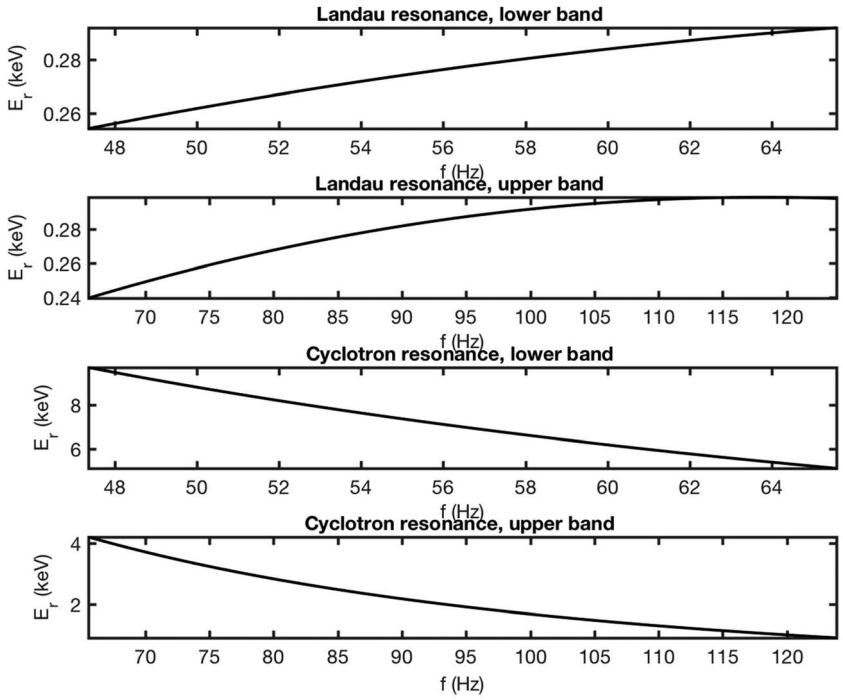

Figure 10. Curves representing the energy resonances, as a function of frequency, for upper and lower band chorus at oblique angles. The top two panels are for Landau resonance, and the bottom two for cyclotron resonance. For the lower band waves, we have used $\theta_N = 63°$, and for the upper band waves we have used $\theta_N = 46°$.

$\theta_N = 46°$. From these curves we see that the parallel electron beams in Figure 9 with energies up to 300 eV are capable of Landau resonance with both the lower and upper band waves, and that the 1-keV beam is capable of cyclotron resonance with the upper band waves. The >2-keV beam does not appear to have the positive anisotropy necessary for a beam cyclotron resonance, and its energy is too high for the Landau resonance.

The wave can also return energy to the electrons—including the residual parallel beams that remain after partitioning energy to the wave growth (Tripathi et al., 2017). The growth rate profiles factor into the scattering efficiency of the waves. We follow the methods detailed in Tripathi and Singhal (2009) and Tripathi et al. (2017) to numerically derive the diffusion coefficients for the wave scattering. The bounce-averaged electron scattering (pitch angle) diffusion rates $D_{\alpha\alpha}$ reveals that the scattering effect of the observed chorus whistler waves exceeds that of the ECH waves observed in burst by THEMIS E. The mean wave spectral power is ~1.5 $\times 10^{-4}$ nT^2/Hz for the upper band chorus and ~2 $\times 10^{-4}$ nT^2/Hz for the lower band chorus. (The wave amplitude exceeds the pT amplitude customarily observed at $L > 8$.) We determine the wave amplitudes from Gaussian fits to the Fourier spectrum of lower band (0.1–0.5)f_{ce} and upper band (0.5–0.8)f_{ce} chorus emissions. As in Tripathi et al. (2017), $D_{\alpha\alpha} \sim \omega_{ce} B_w^2/B_0^2$, where B_w is the wave amplitude and B_0 is the background field magnitude. In the pitch angle diffusion calculations, we have included Landau resonance ($n = 0$) and cyclotron resonances (+1 + 2 + 3 + 4 + 5 and −1 − 2 − 3 − 4 − 5). Tripathi et al. (2017) show that the lower cutoff energy for scattering electrons decreases when ω_{pe}/ω_{ce} increases—for example, the scattering cutoff for lower band chorus lies below 2.5 keV for $\omega_{pe}/\omega_{ce} \sim 4.77$ and below 500 eV for $\omega_{pe}/\omega_{ce} \sim 12$. In the present data, $\omega_{pe}/\omega_{ce} \sim 17.5$, enabling scattering even below 500 eV. Whistler scattering remains significant for electron pitch angles up to about 60° at $\omega_{pe}/\omega_{ce} \sim 12$.

In Figure 11 we plot $D_{\alpha\alpha}$ as a function of pitch angle for ECH waves, and for whistler waves propagating at the two propagation angles found for lower and upper band chorus. We plot different curves for 1- and 2-keV electrons for ECH waves, and for 270 and 500 eV and 1 and 2 keV electrons for whistlers. We have included curves for two magnetic field amplitudes, one observed by THEMIS D (12.11 nT) and the other by THEMIS E (18.77 nT). With $B_0 \sim 12$ nT, we find that at 1 keV $D_{\alpha\alpha} \sim 0.15$ s^{-1} for the upper band chorus (using $\theta_N \sim 45°$) and 0.17 s^{-1} for the lower band chorus (using $\theta_N \sim 60°$, approximately the same as found for parallel

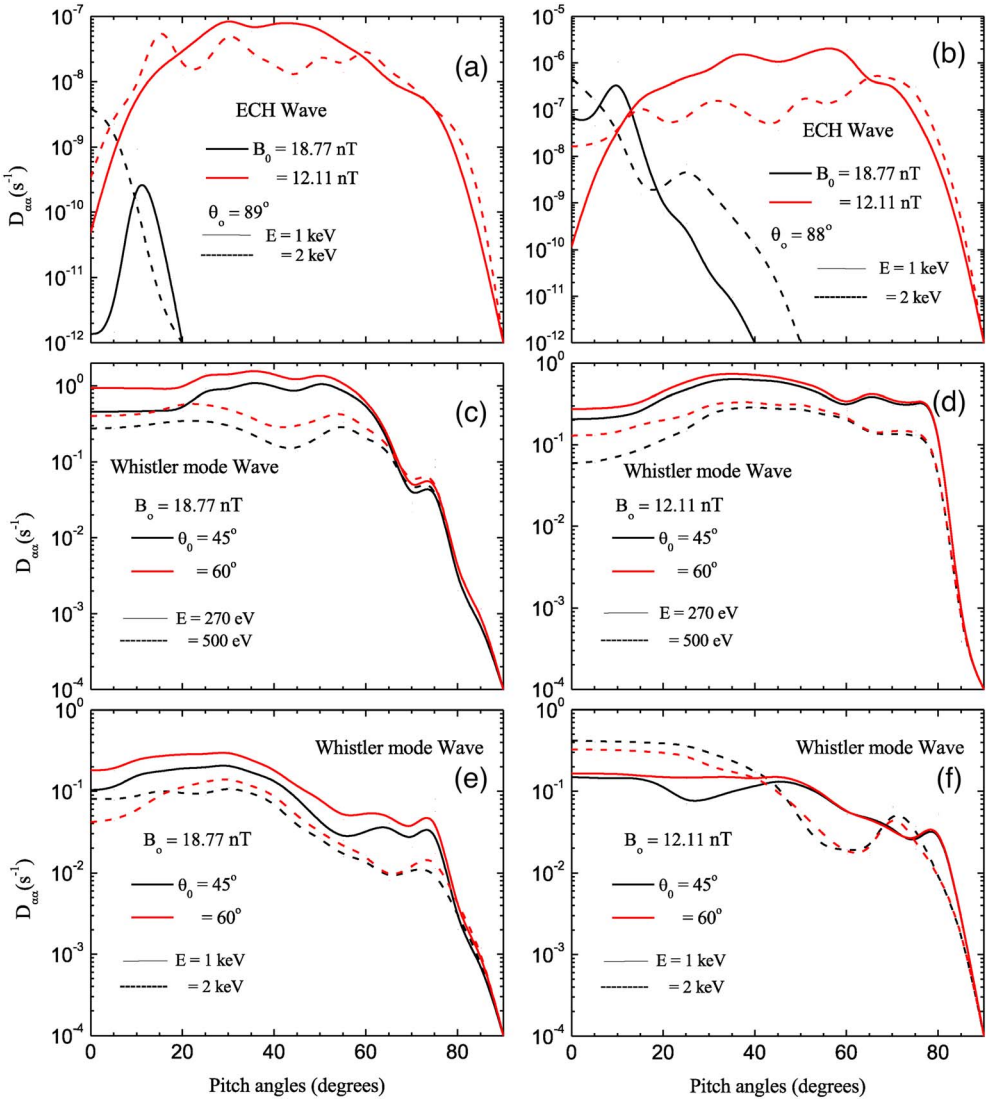

Figure 11. (a) Pitch angle diffusion coefficient ($D_{\alpha\alpha}$) versus pitch angle for ECH waves at two electron energies: 1 keV (solid line) and 2 keV (dotted line), corresponding to two values of ambient magnetic field B_o = 18.77 nT (black curve) and 12.11 nT (red curve); for ECH wave propagation angle θ_o = 89°. (b) Same as Figure 11a but for θ_o = 88°. (c) $D_{\alpha\alpha}$ versus pitch angle for whistler mode waves at two electron energies: 270 (solid line) and 500 eV (dotted line), corresponding to two wave propagation angles θ_o = 45° (black curve) and 60° (red curve); for ambient magnetic field B_o = 18.77 nT. (d) Same as in Figure 11c but for B_o = 12.11 nT. (e) $D_{\alpha\alpha}$ versus pitch angle for whistler mode waves at two electron energies: 1 (solid line) and 2 keV (dotted line), corresponding to two wave propagation angles θ_o = 45° (black curve) and 60° (red curve); for ambient magnetic B_o = 18.77 nT. (f) Same as in Figure 11e but for B_o = 12.11 nT.

propagation). We find that whistlers attain scattering rates of ~ 0.1 to 1 s^{-1} for pitch angles up to at least 60°. In contrast, $D_{\alpha\alpha}$ ~10^{-9} s^{-1} for the ECH waves observed by THEMIS E during the fast flows and 10^{-7} s^{-1} for the lower magnetic field. The whistler wave scattering rates are highest for particle energies below 1 keV, and, except for the case of >1-keV electrons and B_0 = 12.11 nT (Figure 11f), the highest rates are for pitch angles between about 20 and 60°. Some electrons in the 1–2 keV beams that were already inside the loss cone may be efficiently scattered out of the loss cone. However, the electrons below 1 keV with pitch angles between ~ 20 and 60° will be scattered into the loss cone at a higher rate than the 1- to 2-keV parallel electrons will be scattered out of it.

Previous reports (Khotyaintsev et al., 2011; Ni et al., 2008; Thorne et al., 2010; Zhima et al., 2015) have demonstrated that, during quiet times, whistler chorus waves scatter electrons more efficiently from the magnetotail at $L < 8$. However, researchers have found that ECH waves scatter electrons more efficiently

at L shells > 8, during quiet times (Liang et al., 2010; Ni et al., 2012; Ni, Thorne, Liang, et al., 2011; Zhang et al., 2015). We believe the presence of bursty bulk flows changes this picture, such that whistler wave electron scattering predominates at $L > 8$. Furthermore, the observation of oblique whistlers is distinct from previous reports of quasi-parallel whistlers arising from electron pancake distributions in fast flows. Electron beam instabilities tend to produce oblique whistlers, while electron temperature anisotropy instabilities more likely produce quasi-parallel whistlers. In the 1-keV electron energy range, oblique whistlers scatter electrons at least as well as parallel whistlers. Inan and Bell (1991) determine that cyclotron or Landau resonant pitch angle scattering of electrons by oblique whistler waves meets or exceeds that by parallel waves. While the cyclotron scattering coefficient does not peak until θ_N approaches the resonance cone and decreases slightly for the wave normal angles we observe, the Landau resonance scattering coefficient increases dramatically and is resonant with ~1-keV electrons. This finding is reflected also in the results of Ni, Thorne, Meredith, et al., 2011where upper band chorus diffusion coefficients derived from magnetic field measurements are insensitive to wave normal angle, but lower band chorus diffusion coefficients increase considerably for oblique angles, especially for ~1-keV electrons. Ni, Thorne, Meredith, et al. (2011) explain that, for a given wave frequency, the lowest resonant electron energy decreases with increasing chorus wave normal angle, allowing 270 eV to 2 keV electrons to resonate with oblique lower band emissions through Landau or cyclotron resonance. Moreover, although overall wave power may be weaker for larger wave normal angles than for parallel propagation, oblique lower band emissions distribute more energy at the oblique propagation angles. Therefore, they are capable of scattering 1-keV electrons as efficiently as parallel chorus.

Thus, with the oblique chorus propagation, one can expect pitch angle diffusion of electrons over a broad range of initial pitch angles in the energy range that corresponds to precipitation that produces 630-nm diffuse aurora. In strong diffusion, the electron loss cone is almost filled. In this case, $D_{\alpha\alpha} >> \gamma\alpha^2_0$, where α_0 is the loss cone angle, and γ is the loss rate $v_{e,\|}/l$, with l the field line length (Melrose, 1986, after Kennel, 1969). With $\alpha_0 \sim 1°$ and $l \sim 1.1 \times 10^5$ km, strong diffusion of 500-eV electrons into the loss cone requires $D_{\alpha\alpha} >> 0.12\ s^{-1}$. From Figure 11, diffusion of, for example, 500-eV electrons is an order of magnitude larger than $0.12\ s^{-1}$ for pitch angles up to 60° when $B = 18.77$ nT. When $B = 12.11$ nT, it is the same order of magnitude as $0.12\ s^{-1}$. Therefore, the data of these strong flows is consistent with moderate to strong diffusion into the loss cone.

EFI and SCM data acquired at particle burst time resolution allows us to expand our time horizon to include the entire 10-min bursty bulk flow interval at reduced time resolution. Particle burst data go only to ~126 Hz, or 63 Hz Nyquist frequency. Though we cannot resolve ECH waves (f_{ce} is above 300 Hz), we can nevertheless detect the lower portion of whistler branches and thus obtain the occurrence distribution of whistler waves throughout the interval. In Figure 12, the THEMIS D SCM and EFI spectra over the 10-min interval succeeding 05:25:35 UT reveals persistent electromagnetic activity at whistler frequencies during the fast flows. The low-resolution spectrum looks like hiss, but the higher-resolution wave burst data, as in Figures 3, 6, and 7, expose distinct chorus structures. The MVA applied to two subintervals (05:31:40.40–05:31:47.47 and 05:33:16.16–05:33.19.19) again reveals highly oblique wave normal angles ~ 50° and 60°, respectively. THEMIS E captures similar structures. We therefore infer that the oblique whistler waves are present throughout the entire bursty bulk flow interval.

We use FBK data to expand the time horizon to the entire fast flow interval and frequencies up to almost 6 kHz. Furthermore, from FBK data we can infer the distribution and frequencies of electromagnetic (EM) and electrostatic (ES) wave activity within the general vicinity of $L = 11$, including not only the bursty bulk flows but also the relatively quiet periods before and after. The FBK, electric (EDC) and magnetic (SCM) spectra from THEMIS D and THEMIS E during an interval before, during, and after the fast flows are presented in Figure 13. For our data, the six frequency bands have the following minimum, center, and maximum frequencies: (1.26, 2.26, 3.57); (2.52, 4.53, 7.13); (20.1, 36.2, 57.0); (80.2, 144.2, 227.4); (316.0, 572.0, 904.0); and (1390.0, 2689.0, 5994.0) Hz. For the interval during the flows, THEMIS D sees EM waves at frequencies consistent with whistler chorus at 05:29–05:35 (within the white box). THEMIS E also sees EM waves, for example, at 05:32 and right before 05:34. These shared electric and magnetic excitations extend up to the band centered around 144.2 Hz, which is consistent with the whistler wave observations. Both spacecraft also see ES (in this environment, presumably ECH) waves, evident from intervals with ES

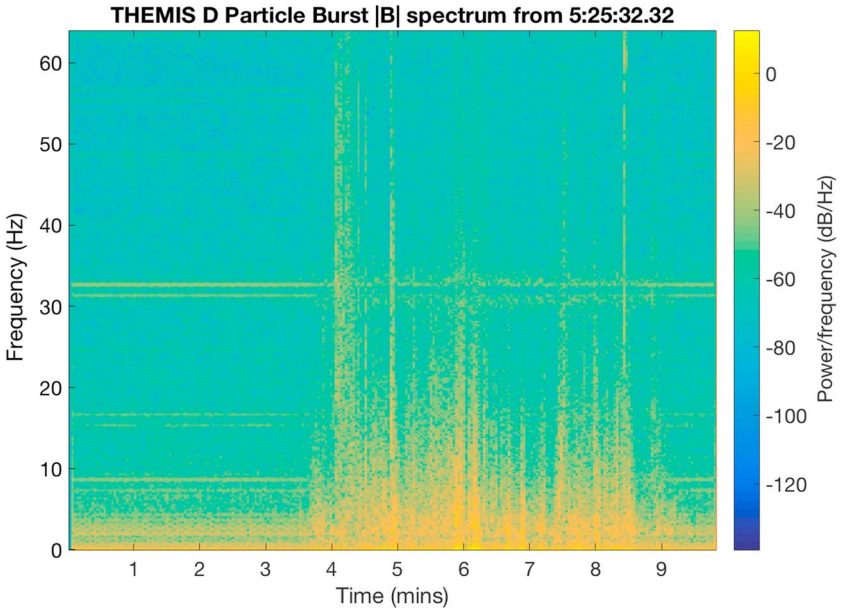

Figure 12. The magnetic spectral intensity acquired from the THEMIS D particle burst-rate data for the entire interval of fast flows, beginning at ~ 05:25:32.32. The electric field data reveal similar activity between the ion (< 1 Hz) and electron cyclotron frequencies (~ 330 Hz). The dispersive electromagnetic emissions are very similar to those detected during the THEMIS D wave burst interval of Figure 5. Lower instrument time resolution (128 Hz) contributes to the appearance of noise and hiss. The beginning of this whistler chorus activity coincides with the first dipolarization of Figure 5.

wave frequencies above about 300 Hz that do not share a magnetic counterpart, for example, near 05:32 and 05:34 on THEMIS D, and 05:30 on THEMIS E, as well as times before and after the fast flows.

There is evidence from FBK that, during the bursty bulk flows, the intensity of the whistler waves exceeds that of the ECH waves, as found from the diffusion coefficients during the wave burst-rate intervals. For example, during the fast flow period, the THEMIS D EFI detects several ES waves in the band centered on 572 Hz that have much lower amplitude than the EM waves detected at lower frequencies by the same instrument. (Here we note, for purposes of comparison to the burst data spectra, that the magnitudes reported in FBK spectra are not recorded in units of spectral power but rather in amplitudes [mV/m and nT]). This adds further evidence to support the hypothesis that the whistler contribution is at least as important as the ECH contribution to electron scattering throughout the entire bursty bulk flow interval.

At times before and after the flows, FBK shows that ES waves occur more frequently than EM waves. Given the location and the observed frequencies, we infer the ES waves are ECH, and the EM waves are whistler chorus. It can be seen in Figure 13 that there are ES waves outside of the fast flow interval. THEMIS D, for example, observes them at around 05:05 and 05:47 UT, while THEMIS E detects them at various times before 05:25 UT and after 05:40 UT. The ES wave frequencies lie in the bands centered on 144.5 and on 572 Hz, primarily about 572 Hz, within the expected ECH range. This observation aligns with the general research consensus that beyond $L = 8$ ECH waves provide the scattering mechanism for diffuse aurora in the absence of fast flows.

The fourth and fifth panels of Figure 2 show the electron energy flux at energies between 31 and 700.5 keV, and up to 30 keV, respectively. As the fast flows continue, the energy bands above 30 keV continue to fill up with an increasing number of electrons, even though the overall number of electrons remains lower than in the ambient plasma sheet. The electrons also become hotter than they were, and their pitch angles become more isotropic. However, the electrons are not heating, since the overall electron temperature is lower than outside the fast flows. Later in the fast flows (~ 5:31:00), the electron pitch angle distributions are hotter and more isotropic, which may be a manifestation of pitch angle diffusion. More perpendicular pitch angles could also result from increasing betatron acceleration, since the magnitude of the magnetic field is also stronger. The presence of whistlers throughout the interval and the scattering efficiency of the chorus evaluated in depth at 05:29:19 together suggest oblique whistlers are the predominant scattering mechanism

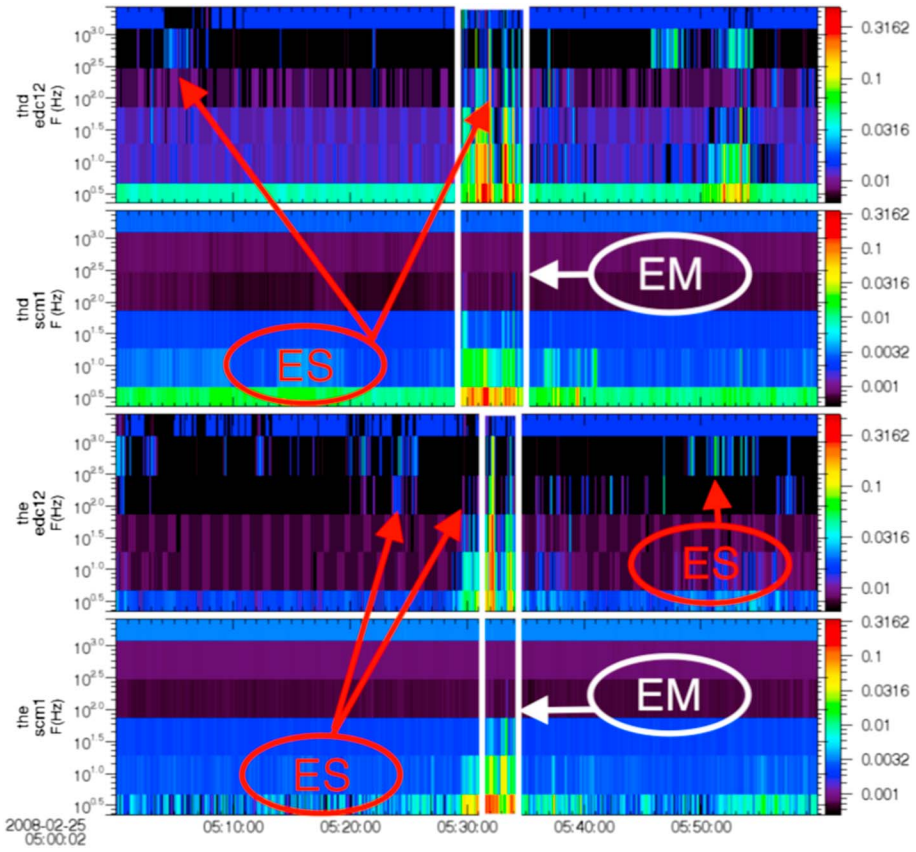

Figure 13. The filterbank (FBK) electric (EDC) and magnetic (SCM) spectra from THEMIS D and THEMIS E during an interval before, during, and after the fast flows. The white box contains an interval with several instances of electromagnetic (EM) waves with frequencies that reach into the band that contains the electron cyclotron frequency (~ 300 Hz), consistent with whistler waves. The red arrows point to times where wave activity is purely electrostatic, in frequency bands ($\gtrsim$ 300 Hz) consistent with ECH waves. These include times within and outside the fast flows.

during the fast flows. Kepko et al. (2009) note that the diffuse 630-nm emission they observe in the auroral region is consistent with enhanced flux and energy of plasma sheet electrons, and Rees and Roble (1986) demonstrate that 0.1- to 2-keV electrons can produce significant 630-nm emissions at the 120- to 360-km altitude range (see their Figure 4).

4. Interpretation and Discussion

During the brief intervals THEMIS D and E take SCM and EFI burst measurements in the bursty bulk flows, THEMIS D captures intense rising tone chorus whistler waves (as seen in Figures 6 and 7), while THEMIS E captures ECH waves. The wave activity is associated with disturbances to the electron density, temperature, and energy. THEMIS encounters a less dense, more energetic electron population in the fast flows. Electron scattering coexists with intervals of waves, suggesting interactions with the waves. During a burst data interval, THEMIS D detects whistler chorus emissions that occur roughly every ~ 0.3–0.4 s and propagate at oblique angles. In one wave, lower band chorus propagates at ~ 63° and upper band chorus at 46°, in this instance. The intervals with intense whistler activity are characterized by parallel electron beams and electron $T_{e,||} > T_{e,\perp}$, in contrast to the pancake anisotropy of previous whistler observations in fast flows. In the flows, the whistler waves are more ubiquitous than the ECH waves, and in the analysis of wave burst intervals of whistler and ECH observations, the whistlers prove more effective at scattering electrons. The diffusion coefficients calculated from the corresponding spectral density profiles reveal that the burst whistler waves measured at THEMIS D have a much stronger electron scattering effect than the burst ECH waves measured by THEMIS E (~ 10^{-3} for whistlers and 10^{-10} for ECH). Over longer periods, with lower-resolution particle burst waveform and slow-survey FBK spectral data, both spacecraft

detect electromagnetic disturbances consistent with whistler waves during the bursty bulk flows. These whistler waves have greater intensity than the ECH waves. The strong ECH emissions inferred from FBK data exist before, during, and after the bursty bulk flows, while the whistler chorus emissions appear only during the bursty bulk flows, supporting previous work arguing for a connection between the two. Thus, we conclude that, in spite of being at distances greater than $L = 8$, the whistler chorus plays the more important role in producing the diffuse aurora during tail substorm events with strong earthward flows and dipolarization fronts.

Our observations of whistler wave production in fast flows differ from most previous observations (e.g., Khotyaintsev et al., 2011; Santolik, 2008; Zhima et al., 2015). Previous works locate whistlers at the edges of magnetic holes (Zhima et al., 2015) and within the flux pileup regions (e.g., Deng et al., 2010; Khotyaintsev et al., 2011) that are characterized by electron betatron acceleration. In these works, a temperature anisotropy $T_{e,\perp}/T_{e,||} > 1$ (pancake distribution) provides the source of free energy for the whistler waves. Though also concurrent with dipolarization, the electron distributions through most of the observations of this work are cigar shaped ($T_{e,\perp}/T_{e,||} < 1$), commonly a signature of Fermi acceleration (Fu et al., 2011). Following stretching of field lines, dipolarization can shrink the length of the field line. Through conservation of the electrons' second adiabatic invariant $v_{e,||}dl$, as the field line length dl shrinks, $v_{e,||}$increases through Fermi acceleration. In a study of ion heating at earthward propagating magnetotail dipolarization fronts, Hwang et al. (2014) similarly conclude that electron beams produced by Fermi acceleration at dipolarization fronts generate low-frequency whistler waves. However, their intent was to link the role of the resulting whistler waves to ion heating behind dipolarization fronts.

The occurrence of either pancake or cigar distributions depends on whether the dipolarized field line relaxes (allowing Fermi acceleration to dominate) or whether it remains compressed by flux pileup (so that betatron acceleration dominates). Fu et al. (2011) propose different electron temperature anisotropies depending on whether the magnetic flux pileup is growing or decaying. Based on evidence from Cluster observations (Deng et al., 2010; Fu et al., 2011), they argue that the electron distributions become cigar shaped from Fermi acceleration when the peak in the earthward perpendicular plasma flow velocity precedes or coincides with the dipolarization in B_z, allowing the dipolarized field line to relax and shrink. In this case, the flux pileup succeeding dipolarization decays. Electron distributions become pancake shaped when the dipolarization in B_z precedes the peak in the perpendicular flow velocity (a dipolarization followed by a growing flux pileup). In the latter case, flux continues to pile up after the dipolarization, the incoming magnetic field being swept in faster than the field lines ahead of it. From conservation of the electrons' first adiabatic invariant $\mu \sim v_{e,\perp}{}^2/B$, $v_{e,\perp}$ must increase when the compression of B_z continues. In either case, since we expect the field line to experience some degree of contraction at a dipolarization unless it is highly compressed, we would also expect to see some degree of Fermi acceleration, even if betatron acceleration dominates. Consequently, we argue that the importance of Fermi acceleration also depends on initial conditions and on the nature of the fast flows. Some observations, for example, have noted Fermi-type acceleration at lower energies (below ~ 5 keV), and betatron type at higher energies (for example, Apatenkov et al., 2007 and THEMIS C observations in Deng et al., 2010). In other observations, betatron acceleration appears to dominate at all energies (Fu et al., 2011 and THEMIS B data in Deng et al., 2010). If initially $v_{e,||}$is small, for example, then its effects may not be significant compared to betatron acceleration. This raises the importance of the initial parallel acceleration of electrons by processes such as reconnection occurring downstream of the fast flows. Moreover, as Liang et al. (2012) have discovered, the electron anisotropy may vary with the intensity of the fast flows. However, the data in this study meet their criteria for fast flows, with the exception that in this event B_z undergoes only one clear dipolarization. Their *dipolarization-dominated* criterion might bring larger magnetic field magnitude increases into their selection pool.

There are indications that Fermi acceleration should be occurring. First, the electron thermal speed ~ 10^4 is much greater than the Alfvèn speed v_A (~10^2–10^3), consistent with a regime where the electron cyclotron and bounce motion are adiabatic (except for the small fraction of electrons scattered into the loss cone). Furthermore, the relationship between the earthward bulk flow, $v_{i,\perp,x}$, B_z, and the electron anisotropy $A = 2T_{e,||}/(T_{e\perp,1} + T_{e\perp,2})$ supports adiabatic behavior and Fermi acceleration. Figure 6 compares the fluctuations in A and B_z (top panel) against the fluctuations in $v_{i,\perp,x}$ (bottom panel) over a time interval that includes the

wave burst data from THEMIS D (where we calculate the fluctuations by subtracting the mean over the interval). The plotted interval begins with the dipolarization in B_z. The shaded intervals denote where the combination of $v_{ix,\perp}$ and B_z is expected to favor Fermi acceleration over betatron acceleration. The second shaded interval corresponds to the THEMIS D wave burst interval from Figure 5. The betatron effect is expected to dominate when flux is piling up, which occurs when the field has already dipolarized (i.e., where B_z has peaked and either remains steady or declines), but the earthward bulk flow perpendicular to **B** is still growing. If B_z is growing, and $v_{i,\perp,x}$ either declines, or grows but peaks at the same time as B_z, then the flux pileup is relaxing, and Fermi acceleration can occur. In all these shaded areas, there is an increase in A, consistent with Fermi acceleration.

We propose a physical scenario as follows. As the first fast flows arrive at THEMIS D at ~ 05:28:50 (Figures 2 and 6), they are followed by a dipolarization in B_z at ~ 05:29:18 (Figure 5, third panel, black curve, marked by solid vertical line). This dipolarization is accompanied by a brief dropout in electrons of all energies until ~ 05:29:24 (Figure 2, fourth and fifth panels), by strong field-aligned electron fluxes at energies up to ~ 3 keV (Figure 2, fifth and eighth panels), and by whistler chorus emissions (Figure 12). (There are subsequent B_z enhancements, but, since they rise more slowly, it is not clear whether they are dipolarizations). There are other intervals of dropouts in electrons at all energies (Figure 2, fourth and fifth panels). There is a brief delay between the first dipolarization and a peak in the earthward perpendicular velocity where flux pileup grows. Subsequently, as B_z remains high but $v_{i,x\perp}$ decreases, the flux-pileup decays while dipolarization remains strong. The parallel electron fluxes and perpendicular flows are therefore consistent with Fermi acceleration of electrons that are already propagating with an initial $v_{e,||}$along field lines, possibly from reconnection down the tail. The field-aligned fluxes grow stronger at ~ 05:29:27. The electron distributions taken during burst mode (Figure 9) reveal parallel beams ~ 500 eV to 3 keV. The apparent increase in parallel electron temperature reflects the presence of parallel and counter-streaming electron beams.

The low-energy, parallel electron beams provide a free-energy source to produce oblique whistler chorus. The beams below 1 keV meet the criterion for Landau resonance, while the 1 keV can undergo cyclotron resonance. We believe the oblique whistlers are produced locally by the observed parallel beams, because THEMIS is located at only about 7° magnetic latitude and because the THEMIS only observes the waves within the fast flows. Chen et al. (2013) and Artemyev et al. (2013) do observe parallel whistlers that later become oblique after they propagate, but this occurs only once the waves are close to 30° latitude. Oblique whistler chorus waves in turn resonate with and scatter low-energy electrons with a wide range of pitch angles into the loss cone. While some fraction of the parallel beams may already precipitate into the loss cone without the need for scattering, some fraction will be scattered out of the loss cone, especially above 1 keV (Figure 11). However, the wave scattering will certainly contribute to the number and energy range of particles within the loss cone. The scattering efficiency is highest for energies <1 keV and for electrons with pitch angles between approximately 20 and 60°. The overall drop and variation in electron temperature at the dipolarization suggest that the dipolarized flux tubes are cooler and perhaps flapping across the spacecraft. While the Fermi process "heats" the electrons in the parallel direction in the dipolarized flux tubes, the overall electron temperature is nevertheless lower than in the undisturbed preflow population. It is possible that the beams' production of chorus waves accounts for some of the electrons' net thermal energy loss relative to preflow values.

This interpretation is sympathetic to the observed timing of the diffuse auroral signatures arising from the fast flows. In their Figure 1, using the Tsyganenko 2002 model, Kepko et al. (2009) map the footpoint of THEMIS D onto the field of view of the THEMIS all-sky imager at Gillam. The 630-nm wavelength imager detects the diffuse aurora brightening, propagating equatorward as the tail flows move earthward. We estimate from the figure that the brightening diffuse aurora reaches the footpoint of THEMIS D at about 05:29:14 UT at the earliest and is definitely visible there by 05:29:34. Assuming a back of the envelope estimated field line length of ~ 1.1×10^5 km for this L shell, the time it would take a 1-keV electron to reach the ionosphere would be ~ 6 s. This is consistent with the arrival time window at the THEMIS D footpoint and with the first whistler observations at THEMIS D at ~ 05:29:18. Of course these estimates and the mapping of the spacecraft position are rough but yield credibility to the association between the whistler observations and the diffuse aurora.

5. Conclusions

We have demonstrated that not only betatron acceleration but also Fermi acceleration can generate whistlers in fast flows. We have also shown that the oblique whistlers thus created play the dominant role in scattering electrons out of the plasma sheet during fast tail flows. In fact, the evidence here, and in other research (Inan & Bell, 1991; Ni, Thorne, Meredith, et al., 2011) of oblique whistler waves more generally, is that the oblique whistlers that are preferred by electron beam instabilities preferentially scatter electrons below 2 keV—the energy range of the diffuse aurora. This is largely through the proclivity of oblique whistlers to Landau resonate with electron beams below 1 keV and to cyclotron resonate with beams at approximately 1 keV. Thus, the Fermi acceleration of electrons through the shrinking of flux tubes at dipolarization fronts provides a mechanism for the coupling of fast flows to the diffuse electron aurora. Processes such as tail reconnection prime the electrons by imparting the initial parallel velocities. A comparison of the diffuse aurora during fast flows dominated by either Fermi or betatron electron acceleration would form an interesting future topic of investigation.

Acknowledgments
This work was supported by NASA grant NNH14ZDA001N-HSR. We used SPEDAS V3.1, (see Angelopoulos et al., 2019) for some data access and processing. The Satellite Situation Center Web (SSCWeb) at NASA GSFC provided the orbit view. THEMIS data used in this study are available to the public through UC Berkeley at http://themis.ssl.berkeley.edu/index.shtml.

References

Angelopoulos, V., Baumjohann, W. J., Kennel, C. F., Coroniti, F. V., Kivelson, M. G., Pellat, R., et al. (1992). Bursty bulk flows in the central plasma sheet. *Journal of Geophysical Research*, *97*(A4), 4027. https://doi.org/10.1029/91JA02701

Angelopoulos, V., Cruce, P., Drozdov, A., Grimes, E. W., Hatzigeorgiu, N., King, D. A., et al. (2019). The space environment data analysis system. *Space Science Reviews*, *215*(1), 9. https://doi.org/10.1007/s11214-018-0576-4

Angelopoulos, V., Kennel, C. F., Coroniti, F. V., Kivelson, M. G., Pellat, R., Walker, R. J., et al. (1994). Statistical characteristics of bursty bulk flow events. *Journal of Geophysical Research*, *99*(A11), 21,257. https://doi.org/10.1029/94JA01263

Angelopoulos, V., McFadden, J. P., Larson, D., Carlson, C. W., Mende, S. B., Frey, H., et al. (2008). Tail reconnection triggering substorm onset. *Science*, *321*(5891), 931–935. https://doi.org/10.1126/science.1160495

Apatenkov, S. V., Sergeev, V. A., Kubyshkina, M. V., Nakamura, R., Baumjohann, W., Runov, A., et al. (2007). Multi-spacecraft observation of plasma dipolarization/injection in the inner magnetosphere. *Annales Geophysicae*, *25*, 801–814. https://doi.org/10.5194/angeo-25-801-2007

Artemyev, A. V., Agapitov, O. V., Mourenas, D., Krasnoselskikh, V., & Zelenyi, L. M. (2013). Storm-induced energization of radiation belt electrons: Effect of wave obliquity. *Geophysical Research Letters*, *40*, 4138–4143. https://doi.org/10.1002/grl.50837

Baumjohann, W. J., Paschmann, G., & Lühr, H. (1990). Characteristics of high-speed flows in the plasma sheet. *Journal of Geophysical Research*, *95*(A4), 3801. https://doi.org/10.1029/JA095iA04p03801

Bellan, P. M. (2013). Circular polarization of obliquely propagating whistler wave magnetic field. *Physics of Plasmas*, *20*(8). https://doi.org/10.1063/1.4817964

Chen, L., Thorne, R. M., Li, W., & Bortnik, J. (2013). Modeling the wave normal distribution of chorus waves. *Journal of Geophysical Research: Space Physics*, *118*, 1074–1088. https://doi.org/10.1029/2012JA018343

Deng, X., Ashour-Abdalla, M., Zhou, M., Walker, R., El-Alaoui, M., Angelopoulos, V., et al. (2010). Wave and particle characteristics of earthward electron injections associated with dipolarization fronts. *Journal of Geophysical Research*, *115*, A09225. https://doi.org/10.1029/2009JA015107

Evans, D. S. (1974). Precipitating electron fluxes formed by a magnetic field aligned potential difference. *Journal of Geophysical Research*, *79*(19), 2853–2858. https://doi.org/10.1029/JA079i019p02853

Fu, H. S., Cao, J. B., Cully, C. M., Khotyaintsev, Y. V., Vaivads, A., Angelopoulos, V., et al. (2014). Whistler-mode waves inside flux pileup region: Structured or unstructured. *Journal of Geophysical Research: Space Physics*, *119*, 9089–9100. https://doi.org/10.1002/2014JA020204

Fu, H. S., Khotyaintsev, Y. V., André, M., & Vaivads, A. (2011). Fermi and betatron acceleration of suprathermal electrons behind dipolarization fronts. *Geophysical Research Letters*, *38*, L16104. https://doi.org/10.1029/2011GL048528

Fuzikawa, M., Sakanoi, T., Miyoshi, Y., Hosokawa, K., Shiokawa, K., Katoh, Y., et al. (2018). Electrostatic electron cyclotron harmonic waves as a candidate to cause pulsating aurora. *Geophysical Research Letters*, *45*, 12,661–12,668. https://doi.org/10.1029/2018GL080145

Gendrin, R. (1961). Le guidage des whistlers par le champ magnetique. *Planetary and Space Science*, *5*(4), 274–282. https://doi.org/10.1016/0032-0633(61)90096-4

Helliwell, R. A. (1965). *Whistlers and related ionospheric phenomena*. Stanford, Calif: Stanford University Press.

Helliwell, R. A., Carpenter, D. L., Inan, U. S., & Katsufrakis, J. P. (1986). Generation of band-limited VLF noise using the simple transmitter: A model for magnetospheric hiss. *Journal of Geophysical Research*, *91*(A4), 4381–4392. https://doi.org/10.1029/JA091iA04p04381

Henderson, M. G., Reeves, G. D., & Murphree, J. S. (1998). Are north-south aligned auroral structures an ionospheric manifestation of bursty bulk flows? *Geophysical Research Letters*, *25*(19), 3737–3740. https://doi.org/10.1029/98GL02692

Huang, S. Y., Zhou, M., Deng, X. H., Yuan, Z. G., Pang, Y., Wei, Q., et al. (2012). Kinetic structure and wave properties associated with sharp dipolarization front observed by Cluster. *Annales Geophysicae*, *30*(1), 97–107. https://doi.org/10.5194/angeo-30-97-2012

Hwang, K.-J., Goldstein, M. L., F.-Viñas, A., Schriver, D., & Ashour-Abdalla, M. (2014). Wave particle interactions during a dipolarization front event. *Journal of Geophysical Research: Space Physics*, *119*, 2484–2493. https://doi.org/10.1002/2013JA019259

Inan, U. S., & Bell, T. F. (1991). Pitch angle scattering of energetic particles by oblique waves. *Geophysical Research Letters*, *18*(1), 49–52. https://doi.org/10.1029/90GL02476

Jiang, L., Ni, B., Cully, C. M., Donovan, E. F., Thorne, R. M., & Angelopoulos, V. (2012). Electromagnetic ELF wave intensification associated with fast earthward flows in mid-tail plasma sheet. *Annales Geophysicae*, *30*(3), 467–488. https://doi.org/10.5194/angeo-30-467-2012

Kasahara, S., Miyoshi, Y., Yokota, S., Mitani, T., Kasahara, Y., Matsuda, S., et al. (2018). Pulsating aurora from electron scattering by chorus waves. *Nature*, *554*(7692), 337–340. https://doi.org/10.1038/nature25505

Kaur, R., & Pandy, R. S. (2017). Study of oblique propagating whistler mode waves in presence of parallel DC electric field in magnetosphere of Saturn. *Advances in Electromagnetism*, *6*(2), 26–32. https://doi.org/10.7716/aem.v6i2.466

Kauristie, K., Sergeev, V. A., Kubyshkina, M., Pulkkinen, T. I., Angelopoulos, V., Phan, T., et al. (2000). Ionospheric current signatures of transient plasma sheet flows. *Journal of Geophysical Research*, *105*(A5), 10,677–10,690. https://doi.org/10.1029/1999JA900487

Kennel, C. F. (1969). Consequences of magnetospheric plasma. *Reviews of Geophysics*, *7*(1, 2), 379. https://doi.org/10.1029/RG007i001p00379

Kepko, L., Spanswick, E., Angelopoulos, V., Donovan, E., McFadden, J., Glassmeier, K. -H., et al. (2009). Equatorward moving auroral signatures of a flow burst observed prior to auroral onset. *Geophysical Research Letters*, *36*, L24104. https://doi.org/10.1029/2009GL041476

Khotyaintsev, Y. V., Cully, C., Vaivads, A., André, M., & Owen, C. (2011). Plasma jet braking: Energy dissipation and nonadiabatic electrons. *Physical Review Letters*, *106*(16). https://doi.org/10.1103/PhysRevLett.106.165001

Khrabov, A. V., & Sonnerup, B. U. Ö. (1998). Orientation and motion of current layers: Minimization of the Faraday residue. *Geophysical Research Letters*, *25*(13), 2372–2376.

Li, W., Thorne, R. M., Nishimura, Y., Bortnik, J., Angelopoulos, V., McFadden, J. P., et al. (2005). THEMIS analysis of observed equatorial electron distributions responsible for the chorus excitation. *Journal of Geophysical Research*, *115*, A00F11. https://doi.org/10.1029/2009JA014845

Liang, J., Ni, B., Cully, C. M., Donovan, E. F., Thorne, R. M. & Angelopoulos, V. (2012). Electromagnetic ELF wave intensification associated with fast earthward flows in mid-tail plasma sheet. *Annales Geophysicae*, *30*(3), 467488. https://doi.org/10.5194/angeo-30-467-2012

Liang, J., Ni, B., Spanswick, E., Kubyshkina, M., Donovan, E. F., Uritsky, V. M., et al. (2011). Fast earthward flows, electron cyclotron harmonic waves, and diffuse auroras: 17 conjunctive observations and a synthesized scenario. *Journal of Geophysical Research*, *116*, A12220. https://doi.org/10.1029/2011JA017094

Liang, J., Spanswick, E., Nicolls, M. J., Donovan, E. F., Lummerzheim, D., & Liu, W. W. (2011). Multi-instrument observations of soft electron precipitation and its association with magnetospheric flows. *Journal of Geophysical Research*, *116*, A06201. https://doi.org/10.1029/2010JA015867

Liang, J., Uritsky, V., Donovan, E., Ni, B., Spanswick, E., Trondsen, T., et al. (2010). THEMIS observations of electron cyclotron harmonic emissions, ULF waves, and pulsating auroras. *Journal of Geophysical Research*, *115*, A10235. https://doi.org/10.1029/2009JA015148

Lilly, J. M., & Park, J. (1995). Multiwavelet spectral and polarization analyses of seismic records. *Geophysical Journal International*, *122*(3), 1001–1021. https://doi.org/10.1111/j.1365-246X.1995.tb06852.x

Lyons, L. R., Nagai, T., Blanchard, G. T., Samson, J. C., Yamamoto, T., Mukai, T., et al. (1999). Association between GEOTAIL plasma flows and auroral poleward boundary intensifications observed by CANOPUS photometers. *Journal of Geophysical Research*, *104*(A3), 4485–4500. https://doi.org/10.1029/1998JA900140

Melrose, D. B. (1986). *Instabilities in space and laboratory plasmas*, (p. 237). Cambridge, UK: Cambridge University Press. https://doi.org/10.1017/CBO9780511564123

Mourenas, D., Artemyev, A. V., Agapitov, O. V., Krasnoselskikh, V., & Mozer, F. S. (2015). Very oblique whistler generation by low-energy electron streams. *Journal of Geophysical Research: Space Physics*, *120*, 3655–3683. https://doi.org/10.1002/2015JA021135

Ni, B., Liang, J., Thorne, R. M., Angelopoulos, V., Horne, R. B., Kubyshkina, M., et al. (2012). *Journal of Geophysical Research*, *117*, A01218. https://doi.org/10.1029/2011JA017095

Ni, B., Thorne, R., Liang, J., Angelopoulos, V., Cully, C., Li, W., et al. (2011). Global distribution of electrostatic electron cyclotron harmonic waves observed on THEMIS. *Journal of Geophysical Research*, *38*, L17105. https://doi.org/10.1029/2011GL048793

Ni, B., & Thorne, R. M. (2012). Recent advances in understanding the diffuse auroral precipitation: The role of resonant wave-particle interactions. In D. Summers, I. R. Mann, D. N. Baker, & M. Schulz (Eds.), *Dynamics of the Earth's radiation belts and inner magnetosphere*, *Geophysical Monograph Series* (pp. 291–301). Washington DC: American Geophysical Union.

Ni, B., Thorne, R. M., Meredith, N. P., Shprits, Y., & Horne, R. B. (2011). Diffuse auroral scattering by whistler mode chorus waves: Dependence on wave normal angle distribution. *Journal of Geophysical Research*, *116*, A10207. https://doi.org/10.1029/2011JA016517

Ni, B., Thorne, R. M., Shprits, Y. Y., & Bortnik, J. (2008). Resonant scattering of plasma sheet electrons by whistler-mode chorus: Contribution to diffuse auroral precipitation. *Geophysical Research Letters*, *35*, L11106. https://doi.org/10.1029/2008GL034032

Pandey, R. S., & Misra, K. D. (2002). Excitation of oblique whistler waves in magnetosphere and in interplanetary space at 1 AU. *Earth, Planets and Space*, *54*(2), 159–165. https://doi.org/10.1186/BF03351716

Panov, E. V., Artemyev, A. V., Baumjohann, W., Nakamura, R., & Angelopoulos, V. (2013). Transient electron precipitation during oscillatory BBF braking: THEMIS observations and theoretical estimates. *Journal of Geophysical Research: Space Physics*, *118*, 3065–3076. https://doi.org/10.1002/jgra.50203

Park, J., Vernon, F. L. III, & Lindberg, G. R. (1987). *Journal of Geophysical Research*, *92*(B12), 12,664–12,674. https://doi.org/10.1029/JB092iB12p12664

Rees, M. H., & Roble, R. G. (1986). Excitation of the O(1D) atoms in aurorae and emission of the [OI] 6300-A° line. *Canadian Journal of Physics*, *64*(12), 1608–1613. https://doi.org/10.1139/p86-284

Santolik, O. (2008). New results of investigations of whistler-mode chorus emissions. *Nonlinear Processes in Geophysics*, *15*(4), 621–630. https://doi.org/10.5194/npg-15-621-2008

Santolik, O., Gurnett, D. A., Pickett, J. S., Chum, J., & Cornilleau-Wehrlin, N. (2009). Oblique propagation of whistler mode waves in the chorus source region. *Journal of Geophysical Research*, *114*, A00F03. https://doi.org/10.1029/2009JA014586

Sauer, K., & Sydora, R. D. (2010). Beam-excited whistler waves at oblique propagation with relation to STEREO radiation belt observations. *Annales Geophysicae*, *28*, 1317–1325. https://doi.org/10.5194/angeo-28-1317-2010

Sergeev, V. A., Liou, K., Meng, C. -I., Newell, P. T., Brittnacher, M., Parks, G., & Reeves, G. D. (1999). Development of auroral streamers in association with localized impulsive injections to the inner magnetotail. *Geophysical Research Letters*, *26*(3), 417–420. https://doi.org/10.1029/1998GL900311

Sergeev, V. A., Liou, K., Newell, P. T., Ohtani, S.-I., Hairston, M. R., & Rich, F. (2004). Auroral streamers: Characteristics of associated precipitation, convection and field-aligned currents. *Annales Geophysicae*, *22*(2), 537–548. https://doi.org/10.5194/angeo-22-537-2004

Sergeev, V. A., Sauvaud, J. . A., Popescu, D., Kovrazhkin, R. A., Liou, K., Newell, P. T., et al. (2000). Multiple-spacecraft observation of a narrow transient plasma jet in the Earth's plasma sheet. *Geophysical Research Letters*, *27*(6), 851–854. https://doi.org/10.1029/1999GL010729

Shi, Y., Zesta, E., Lyons, L. R., Yang, J., Boudouridis, A., Ge, Y. S., et al. (2012). Two-dimensional ionospheric flow pattern associated with auroral streamers. *Journal of Geophysical Research*, *117*, A02208. https://doi.org/10.1029/2011JA017110

Sonnerup, B. Ü. O., & Cahill, L. J. (1967). Magnetopause structure and altitude from Explorer 12 observations. *Journal of Geophysical Research*, *72*(1), 171–183. https://doi.org/10.1029/JZ072i001p00171

Tagirov, V. R., Ismagilov, V. S., Titova, E. E., Arinin, V. A., Perlikov, A. M., Manninen, J., et al. (1999). Auroral pulsations and accompanying VLF emissions. *Annales Geophysicae*, *17*(1), 66–78. https://doi.org/10.1007/s00585-999-0066-9

Terasawa, T., Kawao, H., Shinohara, I., Mukai, T., Saito, Y., Hoshino, M., et al. (1996). On the determination of a moving MHD structure: Minimization of the residue of integrated Faraday's equation. *Journal of Geomagnetism and Geoelectricity*, *48*(5), 603–614. https://doi.org/10.5636/jgg.48.603

Thomson, D. J. (1982). Spectral estimation and harmonic analysis. *Proceedings of the IEEE*, *70*(9), 1055–1096. https://doi.org/10.1109/PROC.1982.12433

Thomson, D. J. (1990). Time series analysis of Holocene climate data. *Philosophical Transactions of the Royal Society of London*, *330*(1615), 601–616. https://doi.org/10.1098/rsta.1990.0041

Thorne, R. M., Ni, B., Tao, X., Horne, R. B., & Meredith, N. P. (2010). Scattering by chorus waves as the dominant cause of diffuse auroral precipitation. *Nature*, *467*(7318), 943–946. https://doi.org/10.1038/nature09467

Tripathi, A. K., & Singhal, R. P. (2009). Diffusion coefficients from resonant interactions with electrostatic electron cyclotron harmonic waves. *Physics of Plasmas*, *16*(11). https://doi.org/10.10163/1.3264735

Tripathi, A. K., Singhal, R. P., & Khazanov, G. V. (2017). Simple analytical expressions for electron pitch angle diffusion coefficients. *Physics of Plasmas*, *24*(3), 032904. https://doi.org/10.1063/1.4978555

Tripathi, A. K., Singhal, R. P., Singh, K. P., & Singh, O. N. II (2013). Diffuse auroral precipitation by resonant interaction with electron cyclotron harmonic and whistler mode waves. *Journal of Atmospheric and Solar-Terrestrial Physics*, *97*, 125–134. https://doi.org/10.1016/j.jastp.2013.01.013

Tsurutani, B. T., Verkhoglyadova, O. P., Lakhina, G. S., & Yagitani, S. (2009). Properties of dayside outer zone chorus during HILDCAA events: Loss of energetic electrons. *Journal of Geophysical Research*, *114*, A03207. https://doi.org/10.1029/2008JA013353

Verkhoglyadova, O. P., & Tsurutani, B. T. (2009). Polarization properties of Gendrin mode waves observed in the Earth's magnetosphere: Observation and theory. *Annales Geophysicae*, *27*(12), 4429–4433. https://doi.org/10.5194/angeo-27-4429-2009

Viberg, H., Khotyaintsev, Y. V., Vaivads, A., André, M., Fu, H. S., & Cornilleau-Wehrlin, N. (2014). Whistler mode waves at magnetotail dipolarization fronts. *Journal of Geophysical Research: Space Physics*, *119*, 2605–2611. https://doi.org/10.1002/2014JA019892

Zesta, E., Donovan, E., Lyons, L., Enno, G., Murphree, J. S., & Cogger, L. (2002). The two-dimensional structure of auroral poleward boundary intensifications (PBIs). *Journal of Geophysical Research*, *107*(A11), 1350. https://doi.org/10.1029/2001JA000260

Zesta, E., Lyons, L. R., & Donovan, E. (2000). The auroral signature of earthward flow burst observed in the magnetotail. *Geophysical Research Letters*, *27*(20), 3241–3244. https://doi.org/10.1029/2000GL000027

Zesta, E., Lyons, L. R., Donovan, E., Frey, H. U., & Nagai, T. (2006). Auroral poleward boundary intensifications and modes of energy transfer in the plasma sheet. *Journal of Geophysical Research*, *111*, A05201. https://doi.org/10.1029/2004JA010640

Zesta, E., Shi, Y., Donovan, E., Spanswick, E., Lyons, L. R., Angelopoulos, V., et al. (2011). Ionospheric convection signatures of tail fast flows during substorms and poleward boundary intensifications (PBI). *Geophysical Research Letters*, *38*, L08105. https://doi.org/10.1029/2011GL046758

Zhang, X. J., Angelopoulos, V., Ni, B., & Thorne, R. M. (2015). Predominance of ECH wave contribution to diffuse aurora in Earth's outer magnetosphere. *Journal of Geophysical Research: Space Physics*, *120*, 295–309. https://doi.org/10.1002/2014JA020455

Zhang, Y. L., Matsumoto, H., & Omura, Y. (1993). Linear and nonlinear interactions of an electron beam with oblique whistler and electrostatic waves in the magnetosphere. *Journal of Geophysical Research*, *90*(A12), 21,353–21,363.

Zhima, Z., Cao, J., Fu, H., Liu, W., Chen, L., Dunlop, M., & Zhang, X. M. (2015). Whistler mode wave generation at the edges of a magnetic dip. *Journal of Geophysical Research: Space Physics*, *120*, 2469–2476. https://doi.org/10.1002/2014JA020786